



UNIVERSITY OF LEEDS

This is a repository copy of *Heterogeneous Multiscale Methods for modelling surface topography in Elastohydrodynamic Lubrication line contacts*.

White Rose Research Online URL for this paper:  
<http://eprints.whiterose.ac.uk/109467/>

Version: Accepted Version

---

**Article:**

De Boer, GN, Gao, L, Hewson, RW et al. (1 more author) (2017) Heterogeneous Multiscale Methods for modelling surface topography in Elastohydrodynamic Lubrication line contacts. *Tribology International*, 113. pp. 262-278. ISSN 0301-679X

<https://doi.org/10.1016/j.triboint.2016.12.019>

---

© 2016 Elsevier Ltd. Licensed under the Creative Commons Attribution-NonCommercial-NoDerivatives 4.0 International  
<http://creativecommons.org/licenses/by-nc-nd/4.0/>

**Reuse**

Unless indicated otherwise, fulltext items are protected by copyright with all rights reserved. The copyright exception in section 29 of the Copyright, Designs and Patents Act 1988 allows the making of a single copy solely for the purpose of non-commercial research or private study within the limits of fair dealing. The publisher or other rights-holder may allow further reproduction and re-use of this version - refer to the White Rose Research Online record for this item. Where records identify the publisher as the copyright holder, users can verify any specific terms of use on the publisher's website.

**Takedown**

If you consider content in White Rose Research Online to be in breach of UK law, please notify us by emailing [eprints@whiterose.ac.uk](mailto:eprints@whiterose.ac.uk) including the URL of the record and the reason for the withdrawal request.



[eprints@whiterose.ac.uk](mailto:eprints@whiterose.ac.uk)  
<https://eprints.whiterose.ac.uk/>

## Heterogeneous Multiscale Methods for modelling surface topography in EHL line contacts

43<sup>rd</sup> Leeds-Lyon Symposium on Tribology, 6<sup>th</sup>-9<sup>th</sup> September 2016, Leeds, UK  
Tribology International

de Boer G N<sup>a\*</sup>, Gao L<sup>b</sup>, Hewson R W<sup>b</sup>, Thompson H M<sup>a</sup>

<sup>a</sup> School of Mechanical Engineering, University of Leeds, Woodhouse Lane, Leeds, LS2 9JT, UK.

<sup>b</sup> Department of Aeronautics, Imperial College London, South Kensington Campus, London, SW7 2AZ, UK.

\* Corresponding author. Email: G.N.deBoer@leeds.ac.uk; Tel: +44(0) 113 343 2220.

### ABSTRACT

A multiscale method for the Elastohydrodynamic Lubrication (EHL) of line contacts is derived based on the Heterogeneous Multiscale Methods. Periodicity applies to the topographical features and lubricant flow, data is homogenised over a range of variables at a micro-scale and coupled into a macro-scale model. This is achieved using flow factors as calculated from metamodels, which themselves evolve with the solution procedure. Results are given for an idealised topography and illustrate significant deviations from smooth surface assumptions as quantified by the flow factors. Improvements in the accuracy and efficiency with previous work and large fluctuations due to micro-EHL are also presented. Validation of the multiscale method with a deterministic topography is provided demonstrating good accuracy and efficiency.

Keywords: EHL; micro-EHL; Surface Topography; Metamodelling.

### 1. INTRODUCTION

The Elastohydrodynamic Lubrication (EHL) of line contacts generates high pressures which result in the bounding surfaces being separated by a thin lubricant film [1]. Surface topography can be of a similar scale to the film thickness and therefore has an effect on the performance of the tribological system [2]. For example Etsion et al. [3] showed that surface features can reduce the contacting friction of an EHL contact and Greenwood and Johnson [4] demonstrated that transverse waviness caused ripples in EHL pressure distributions. Reconciling the disparity in scales between surface topography and the contact region is a challenging computational problem for which many authors have sought solutions. Waviness in EHL has been modelled for example by Hooke [5] and Venner and Lubrecht [6] who investigated the amplitude reduction effect, but no such general method for describing the influence of surface topography in EHL as yet exists. The level of discretisation necessary to successfully solve fully deterministic problems, where both the contact region and surface topography are modelled simultaneously, has led to the development of homogenisation based models [7]. In such models information pertaining to the EHL of a topographical feature is characterised over a range of variables and subsequently coupled into a model for the EHL of the contact region. Periodicity in the lubricant flow and topographical features ensure that homogenisation of the solutions obtained at the smaller scale produces data which represents the behaviour of the larger scale [8, 9]. Solutions to the EHL problem which are deterministic by nature also remain the subject of a significant amount of recent research [10-17].

Patir and Cheng [18] first developed a two-scale model to include the effects of surface topography in hydrodynamic lubrication known as the flow factors method. In this approach the terms of the Reynolds equation, which describes the lubricant flow in the contact under smooth surface assumptions [19], were multiplied by flow factors which include the homogenised effects of surface topography. Sahlin, et al. [20] used flow factors to develop a homogenisation method for analysing hydrodynamic bearings with periodic roughness which was then extended to mixed lubrication [21], however Fluid-Structure Interaction (FSI) was not considered. de Kraker, et al. [22] developed a model based on flow factors to investigate more complex descriptions of lubricant flow than the conventional Reynolds equation such as the Navier-Stokes equations, FSI was only considered for the contacting region and was not examined at the scale of the topographical features. There are a number of recently published papers investigating other homogenisation techniques for EHL which span a range of applications including examining the constitutive equations of lubricant flow [23], cavitation [24], non-conformal contact [25], and soft contact [26].

The Heterogeneous Multiscale Methods (HMM) [27] are a set of general techniques which allows a problem to be described over multiple scales, the approach is applicable when the difference in scales is greater than an order of magnitude and periodicity applies to the geometric and flow features of the smaller scale. Gao and Hewson [28] first developed a framework for EHL and micro-EHL based on the HMM, a pressure gradient – mass flux relationship was derived based on the homogenisation of periodic micro-EHL simulations which was subsequently used to solve the larger scale EHL problem. de Boer, et al. [29] applied the HMM to the EHL of tilted-pad bearings where three-dimensional topography and the Navier-Stokes equations were examined but the pressures generated did not exceed 8 MPa. This approach coupled the scales of the problem using Response Surface Methods (RSM), with periodicity in the topographical features and corresponding lubricant flow

facilitating the assumptions of the HMM. de Boer, et al. [30] furthered the application of RSM to the method and went on to optimise the surface topography to minimise friction in the contacting region, and Gao, et al. [31] investigated the role of micro-cavitation using the method. The HMM have also recently been used to examine real roughness in the pressure-driven flow through two surfaces [32] and in which the uncertainty of the results due to the random nature of topography is investigated.

This work develops the HMM approach for EHL [28-31] in application to line contacts, which have not as yet been investigated using the approach, nonlinearities introduced by piezoviscosity, compressibility, and contact mechanics are accounted for in the model representing a significant numerical challenge. Results are presented for line contacts in which the Hertzian contact pressures reach up to 0.36 GPa, with the development solution procedure using RSM to couple the scale of the problem becoming the focal point of the work. The EHL problem is formulated into an equation including flow factors to describe the influence of surface topography in the contact (micro-EHL), and from which the deviation from smooth surface assumptions is quantified. These flow factors are calculated as the solution procedure converges using a curvilinear discretisation method for selecting the experiments required.

## 2. THEORY

### 2.1 Macro-Scale Model

The macro-scale model considers the EHL of a line contact in which pressure generated in the lubricant causes deformation of the bounding surfaces, this interaction is fully-coupled to reach a prescribed load carrying capacity. In this paper the lower surface of the contact is modelled as smooth and flat, the upper surface is modelled with topography and curvature, the material of the lower surface is much stiffer than the upper such that only elastic deformation of the latter is included. For the current model isothermal operating conditions are specified and the fluid film is assumed to carry the full load imposed such that no asperity contact or mixed lubrication occurs. A diagram of the macro-scale model for the line contact region is given in Fig. 1.

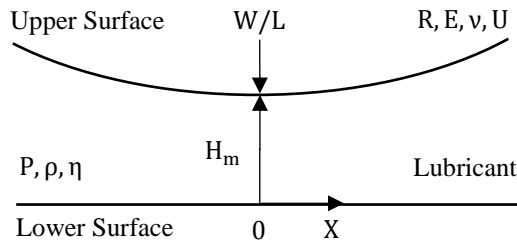


Fig. 1 – Diagram of the macro-scale EHL model.

#### 2.1.1 Macro-Scale Fluid Flow

The macro-scale fluid flow is based on the Reynolds equation for the description of lubricant transport, flow factors are included which are used to tune the response to fit data as determined via homogenisation of the micro-scale model. Eq. (1) is the equation for mass flux  $Q$  in the direction of motion  $X$  which including the continuity equation  $dQ/dX = 0$  becomes Eq. (2), the equivalent Reynolds equation for the macro-scale model [33],

$$Q = -\varphi_1 \frac{\rho(P)}{12\eta(P)} H_m^3 \frac{dP}{dX} + \varphi_2 \rho(P) U H_m \quad (1)$$

$$\frac{d}{dX} \left[ \varphi_1 \frac{\rho(P)}{\eta(P)} H_m^3 \frac{dP}{dX} \right] = 12U \frac{d}{dX} [\varphi_2 \rho(P) H_m] \quad (2)$$

where  $\varphi_1, \varphi_2$  are flow factors,  $P$  is the macro-scale pressure,  $\rho$  is the lubricant density,  $\eta$  is the lubricant viscosity,  $H_m$  is the macro-scale film thickness,  $U$  is the entrainment velocity for which  $U = (U_1 + U_2)/2$  where  $U_1, U_2$  are the velocities of the lower and upper surfaces respectively. Eq. (2) is solved according to the boundary conditions:  $P(-\infty) = P(\infty) = dP/dX(\infty) = 0$ . In the outlet region of the contact the lubricant will cavitate as pressure sharply reduces to absolute zero, a further constraint is applied to model this effect:  $P < 0, dP/dX = 0$ . The vapour phase of the lubricant is not considered, for further work investigating cavitation and application of the HMM for EHL see Gao, et al [31].

#### 2.1.2 Macro-Scale Film Thickness

Eq. (3) describes the film thickness relationship for the macro-scale EHL as the sum of two terms,

$$H_m = H + \frac{P^*}{k} \quad (3)$$

the first  $H$  represents the film thickness in the contact as calculated from the baseline geometry and macro-scale deformation and the second  $P^*/k$  represents the micro-scale deformation where  $P^*$  is the load per unit area and  $k$  is the stiffness per unit area. The film thickness  $H$  is calculated for the line contact from Eq. (4) in which Hertzian contact mechanics describes the macro-scale deformation of the elastic body [33],

$$H = H_0 + \frac{X^2}{2R} - \frac{2}{\pi E'} \int_{-\infty}^{\infty} P^* \ln|X - X'| dX' - \frac{P^*}{k} \quad (4)$$

where  $H_0$  is the separation, and  $R$  is the radius of curvature.  $E'$  is the reduced modulus as determined from the Young's modulus  $E$  and Poisson's ratio  $\nu$  of the solid contacting body:  $1/E' = (1 - \nu^2)/E$ . The term  $P^*/k$  equals the amount of deformation equivalent to that experienced by a spring of stiffness per unit area  $k$  under load per unit area  $P^*$ . This deformation is comparable to that modelled at the micro-scale (see Section 2.2), the term  $H_m$  thus represents the total film thickness of the macro-scale problem.

### 2.1.3 Load Per Unit Area

The load per unit area  $P^*$  differs from pressure  $P$  as a result of the multiscale approach,  $P^*$  is used at the macro-scale to determine deformation and load, whereas  $P$  is used at the macro-scale to solve the fluid flow problem. A further flow factor  $\varphi_3$  is introduced to relate these variables as given by Eq. (5),

$$P^* = \varphi_3 P \quad (5)$$

for a given speed and lubricant the flow factors  $\varphi_1, \varphi_2, \varphi_3$  are homogenised functions of the variables  $dP/dX, P, H$  as given from the micro-scale, see Section 2.2 and Section 2.3. When  $\varphi_1, \varphi_2, \varphi_3 = 1$  the multiscale problem reduces to the case where no topography is considered and smooth surface assumptions apply.

### 2.1.4 Lubricant Properties

Lubricant compressibility is modelled using the barotropic Dowson and Higginson equation, as given by Eq. (6) [34],

$$\rho(P) = \rho_0 \frac{D_0 + D_1 P}{D_0 + P} \quad (6)$$

where  $\rho_0$  is the ambient density, and  $D_0, D_1$  are constants. The lubricant viscosity is modelled using the Roelands equation, the piezoviscous response is described by Eq. (7) [35],

$$\eta(P) = \eta_0 \exp \left[ \ln \left( \frac{\eta_0}{\eta_r} \right) \left( \left( 1 + \frac{P}{p_r} \right)^Z - 1 \right) \right] \quad (7)$$

where  $\eta_0$  is the ambient viscosity,  $\eta_r$  is the reference viscosity,  $p_r$  is the reference pressure, and  $Z$  is the piezoviscous index. Eqs. (6) and (7) were fitted for particular lubricants and have been chosen here to demonstrate the performance of the multiscale method with regard to the effects of compressibility and piezoviscosity in EHL line contacts.

### 2.1.5 Load Capacity

Solving Eq.(2) for pressure and Eq. (4) for film thickness produces the solution to the macro-scale EHL problem, a load  $W$  per unit depth  $L$  is required for the contact as described by Eq. (8),

$$\frac{W}{L} = \int_{-\infty}^{\infty} P^* dX \quad (8)$$

this is achieved by varying the separation  $H_0$  of the contact until the required load is met.

### 2.1.6 Non-Dimensionalisation

Macro-scale variables are non-dimensionalised as is conventional for EHL line contact problems using the half-width of the Hertzian contact  $a = \sqrt{8WR/E'L}$  and the Hertzian contact pressure  $p_h = 2W/\pi aL$  [33]. The macro-scale variables are scaled according to Eq. (9), a full description of the non-dimensional form of the governing equations is given in Appendix A.

$$\overline{P}, \overline{P^*} = \frac{P, P^*}{p_h} \quad \overline{X} = \frac{X}{a} \quad \overline{H}, \overline{H_m} = \frac{(H, H_m)R}{a^2} \quad (9)$$

## 2.2 Micro-Scale Model

The micro-scale model considers the EHL of a subdomain independent of the contact region, a homogenised pressure gradient  $dP/dX$ , pressure  $P$ , and film thickness  $H$  from the macro-scale determine the parameters of the micro-scale model. There is no constraint on the dimension of smaller scale model using HMM so long as periodic conditions apply across all parameters and dimensions [27], a 3D micro-scale model is considered here as shown in Fig.2. The micro-scale model employed is 3D in order to demonstrate how the number of degrees of freedom can be increased from the 2D macro-scale model by the HMM, and as such is developed toward representing surface roughness data obtained experimentally in 3D.

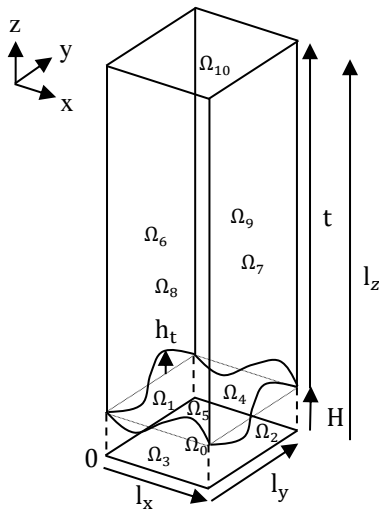


Fig. 2 – Diagram of the micro-scale EHL model.

The dimensions of the subdomain  $l_x, l_y, l_z$  for the coordinate directions  $x, y, z$  depend on the separation of scales in the problem: (i)  $l_x$  and  $l_y$  are required to be at least an order of magnitude or more smaller than the macro-scale contact region; (ii) the micro-scale thickness  $t$  is required to be at least an order of magnitude or more larger than  $l_x, l_y$ . Case (i) defines the size of the micro- and macro-scales, and Case (ii) defines a solid thickness for the micro-scale which represents the stiffness properties required at the macro-scale.

The choice of the length scale representing the macro-scale contact region in Case (i) is an important consideration because this determines the size of applicable micro-scale domains and thus topographies which can be investigated. The full length of the contact includes regions where surface topography will have little influence on the lubrication flow, i.e. toward inlet/outlet where the film thickness is much larger than the size of topography. Therefore it is applicable to use an argument based on the region surrounding the minimum film thickness to represent the region where surface topography will have a significant influence. Here we assume the Hertzian contact region  $2a$  to represent the length of the macro-scale contact region and from which the feasible size of the micro-scale  $l_x$  can be determined,  $\mathcal{O}(l_x) < \mathcal{O}(2a) - 1$ . This separation in scales is similar to that used in deriving Reynolds equation, in which the near-parallel assumption of the contacting surfaces leads to the negation of derivatives across the fluid film. The out-of-plane depth at the micro-scale is constrained to be an order of magnitude or more less than the macro-scale depth,  $\mathcal{O}(l_y) < \mathcal{O}(L) - 1$ . By definition of a line contact the macro-scale depth is considered to be much larger than the length of the contacting region, leading to the negation of derivatives in this direction. Due to periodicity at the boundaries in the micro-scale as the size of the surface topography is reduced to zero then we arrive at the exact value as described by the Reynolds equation for a line contact, and conversely if the size of the surface topography is increased then we move further from the assumption of two near-parallel surfaces in contact.

The thickness of the micro-scale domain  $t$  represents a column of solid material which deforms by an amount equal to that given by a stiffness per unit area  $k$  under a load per unit area  $P^*$ . By constraining the geometry such that  $t$  is greater than  $l_x, l_y$  by at least an order of magnitude,  $\mathcal{O}(t) > \mathcal{O}(l_x, l_y) + 1$ , the column of material can be assumed to act in the  $z$  direction as an equivalent spring of stiffness  $k$ . The thickness  $t$  is subsequently derived from the material properties of the solid column in the longitudinal direction as described in Section 2.2.3.

### 2.2.1 Micro-Scale Fluid Flow

The micro-scale fluid flow is described by Reynolds equation on the lower surface of the subdomain  $\Omega_0$  where  $0 \leq x \leq l_x, 0 \leq y \leq l_y, z = 0$ . The governing equations and lubricant properties of the micro-scale model can take different forms which differ in assumptions from the macro-scale model, such as the Navier-Stokes equations and shear-thinning behaviour, as investigated by de Boer, et al. [29]. In this work we have chosen to keep the assumptions the same as the macro-scale model, with the lubricant density and viscosity described by Eqs. (6) and (7) respectively. Eq. (10) is the Reynolds equation for lubricant transport in the micro-scale model,

$$\frac{\partial}{\partial x} \left[ \frac{\rho(p)}{\eta(p)} h^3 \frac{\partial p}{\partial x} \right] + \frac{\partial}{\partial y} \left[ \frac{\rho(p)}{\eta(p)} h^3 \frac{\partial p}{\partial y} \right] = 12U \frac{\partial}{\partial x} [\rho(p)h] \quad (10)$$

where  $p$  is the micro-scale pressure, and  $h$  is the micro-scale film thickness. Eq. (10) includes the additional leakage term in which gradients in the out-of-plane direction  $y$  must be considered to account for mass conservation at this scale, this is not modelled in the macro-scale by definition of the line contact and instead the solution is based on the mass conservation of homogenised solutions provided by the micro-scale. The solution to Eq. (10) is achieved by specifying boundary conditions for the micro-scale pressure at the extents of the subdomain. In the direction of motion a quasi-periodic condition is imposed  $p_{\Omega_2} = p_{\Omega_1} + \Delta p$  and in the cross-flow direction a standard periodic condition is used  $p_{\Omega_3} = p_{\Omega_4}$ . The variable  $\Delta p$  is the pressure difference over the subdomain in the direction of motion and is determined from the homogenised pressure gradient using Eq. (11),

$$\frac{dP}{dX} = \frac{\Delta p}{l_x} \quad (11)$$

the pressure profile for each set of opposing boundaries will be equal, in the direction of motion the magnitude is shifted by  $\Delta p$ . These periodic boundary conditions combined with a point constraint in the subdomain for the pressure,  $p(0,0) = P + \text{sgn} \Delta p \cdot |\Delta p|/2$ , satisfy the necessary conditions for the HMM. The following constraints are also applied to model the effect of lubricant cavitation in the micro-scale subdomain:  $p < 0, \partial p / \partial x, \partial p / \partial y = 0$ . In the case where  $P + \text{sgn} \Delta p \cdot |\Delta p|/2 < 0$ , the constraint pressure is set to zero. From the periodicity and constraints specified, if the dimensions of the micro-scale fluid domain  $l_x, l_y$  are reduced to zero the solution becomes the exact corresponding solution of Reynolds equation for the values of  $dP/dX, P, H$  specified.

### 2.2.2 Micro-Scale Film Thickness

Film thickness in the micro-scale model is described by Eq. (12),

$$h = H + h_t + w \quad (12)$$

where  $h_t$  is the function describing surface topography, and  $w$  is the micro-scale deformation in the  $z$  direction. The function describing surface topography must be periodic at the extents of the subdomain in both the  $x$  and  $y$  coordinate directions, such that:  $h_{t,\Omega_1} = h_{t,\Omega_2}, h_{t,\Omega_3} = h_{t,\Omega_4}$ . In this work  $h_t$  is chosen such that the mean value must be zero, this condition ensures that for the inclusion of any periodic description of surface topography the change in volume over the subdomain is zero.

### 2.2.3 Micro-Scale Equivalent Spring

Deformation in the micro-scale model is determined from the structural analysis of a column of solid material representing a spring with stiffness per unit area  $k$ . The amount of deformation which this equivalent spring produces is that required by the macro-scale model  $P^*/k$ . It is assumed that the solid column thickness  $t$  is an order of magnitude larger than the remaining dimensions and as such the longitudinal properties of the solid material can be used to represent the thickness of material required in 3D to give a spring of stiffness  $k$ . The thickness  $t$  is derived according to Eq. (13),

$$t = \frac{M}{k} \quad (13)$$

where  $M = E(1 - \nu)/(1 + \nu)(1 - 2\nu)$  is the longitudinal modulus of the solid material.

#### 2.2.4 Micro-Scale Structural Mechanics

A 3D linear elastic model is used to determine the deformation of the equivalent spring, the solid domain is defined by  $0 \leq x \leq l_x, 0 \leq y \leq l_y, H + h_t \leq z \leq l_z$  such that the topography forms the lower surface of the solid. The inclusion of topography does not change the volume of the solid domain meaning that the magnitude of deformation of the equivalent spring will be consistent with the assumptions of the HMM. The deformation vector  $\mathbf{u} = (u, v, w)$  is determined by the solution to Eqs. (14) - (16) [36],

$$\nabla \cdot \boldsymbol{\sigma} = 0 \quad (14)$$

$$\boldsymbol{\sigma} = 2\mu\boldsymbol{\varepsilon} + \lambda \text{tr}(\boldsymbol{\varepsilon}) \quad (15)$$

$$\boldsymbol{\varepsilon} = \frac{1}{2}[\nabla\mathbf{u} + (\nabla\mathbf{u})^T] \quad (16)$$

where  $\boldsymbol{\sigma}$  is the stress tensor,  $\boldsymbol{\varepsilon}$  is the strain tensor, and  $\mu = E/2(1 + \nu)$  and  $\lambda = E\nu/(1 + \nu)(1 - 2\nu)$  are the shear modulus and Lamé's first parameter of the solid material respectively. The boundary conditions required to solve the micro-scale structural problem are defined by the following, where  $\mathbf{n}$  is the normal vector to the surface:  $\boldsymbol{\sigma}_{\Omega_5} \cdot \mathbf{n}_{\Omega_5} = -p_{\Omega_0}\mathbf{n}_{\Omega_5}$ ;  $u_{\Omega_6} = u_{\Omega_7} = v_{\Omega_6} = v_{\Omega_7} = 0$ ;  $u_{\Omega_8} = u_{\Omega_9} = v_{\Omega_8} = v_{\Omega_9} = 0$ ;  $\mathbf{u}_{\Omega_{10}} = 0$ . These constraints load the solid from the lower surface, the sides are all constrained to zero except for in the z direction, and the upper surface is fully constrained. As such the material moves as a spring under load, of which the stiffness per unit area is k. The pressure used to load the surface representing topography is determined from the micro-scale fluid flow at the lower surface of the subdomain. The deformation w used to calculate the film thickness in Eq. (12) relates to the z component on the surface representing topography, the surface deformations under load are mapped to the stationary coordinates of the lower surface to provide deformation over the area of the micro-scale fluid flow domain.

Due to fluctuations in pressure in the fluid domain the deformation w will not be uniformly distributed and as such the film thickness also varies at the micro-scale, this results in the solution moving away from the periodic assumptions used in defining the micro-scale geometry (see Section 2.2.2). The variation in w over the micro-scale solid domain can be assumed small enough in comparison to the spring column deformation  $P^*/k$  such that the resulting deviation from a periodic film thickness is an order of magnitude or more smaller than the total film thickness. This assumption holds so long as the separation in scales associated with defining the thickness of the solid column of material such that it is an order of magnitude larger than the domain length is maintained (see Section 2.2.3). Therefore the solid column thickness t must be an order of magnitude larger than  $l_x$  such that the deformed film thickness is as close to periodic as possible and that the deformation does not effect the boundary conditions of the micro-scale model. For a given definition of surface topography the value of the stiffness per unit area k is chosen in order to satisfy this criteria alone.

#### 2.2.5 Homogenisation

The micro-scale EHL problem is solved by coupling the solution to pressure from Eq. (10) with the deformation from Eqs. (14) - (16), a quasi-static approach is taken such that pressure and deformation are solved iteratively. In order to couple the micro-scale model with the macro-scale, information is homogenised for the micro-scale subdomain and mapped to the solution at the macro-scale. The homogenised micro-scale mass flux  $Q'$  and load per unit area  $P^{*'}$  are determined in the micro-scale fluid domain from Eqs. (17) and (18) respectively,

$$Q' \left( \frac{dP}{dX}, P, H \right) = \frac{1}{l_y} \int_0^{l_y} \left( -\frac{\rho(p)}{12\eta(p)} h^3 \frac{\partial p}{\partial x} + \rho(p)U h \right)_{0,y} dy \quad (17)$$

$$P^{*'} \left( \frac{dP}{dX}, P, H \right) = \frac{1}{l_x l_y} \int_0^{l_y} \int_0^{l_x} p dx dy \quad (18)$$

and are functions of the variables used to characterise the micro-scale  $dP/dX, P, H$ . The line  $x = 0$  is chosen to determine the homogenised mass flux arbitrarily from  $x = l_x$ . The micro-scale variables  $Q'$  and  $P^{*'}$  are approximated at the macro-scale to give  $Q$  and  $P^*$  by calculating the flow factors  $\phi_1, \phi_2, \phi_3$  in Eqs. (1) and (5) respectively. Studying Eqs. (17) and (18) reveals that the multiscale method introduces fluctuations in the mass

flux and load per unit area in the macro-scale model which are functions of the variables solved for at this scale. These fluctuations are caused by the homogenised micro-EHL effect of the micro-scale model in which 3D topography has been introduced.

Further variables are introduced into the model:  $P_{\min}$  is the minimum pressure;  $P_{\max}$  is the maximum pressure;  $H^*$  is the volume per unit area;  $H_{\min}$  is the minimum film thickness; and  $H_{\max}$  is the maximum film thickness. Each of these variables are given by Eqs. (19)-(23) respectively, where the variables followed by dashes are assessed in the micro-scale domain and are subsequently calculated in the macro-scale using the flow factors  $\varphi_{4-8}$ . When  $\boldsymbol{\varphi} = (\varphi_1, \dots, \varphi_8) = 1$  smooth surface assumptions apply, and when  $\boldsymbol{\varphi} \neq 1$  deviations from the smooth surface assumptions due to the effects introduced at the micro-scale are modelled. It is also possible to derive variables investigating the fluctuation in other parameters at the micro-scale and assess them at the macro-scale, such as viscosity or density. Here we do not look individually at these effects and so they have not been defined, but it is of note that they can be investigated using the multiscale method.

$$P_{\min}' \left( \frac{dP}{dX}, P, H \right) = \min_{x,y}(p) \quad P_{\min} = \varphi_4 P \quad (19)$$

$$P_{\max}' \left( \frac{dP}{dX}, P, H \right) = \max_{x,y}(p) \quad P_{\max} = \varphi_5 P \quad (20)$$

$$H^*' \left( \frac{dP}{dX}, P, H \right) = \frac{1}{l_x l_y} \int_0^{l_y} \int_0^{l_x} h \, dx \, dy \quad H^* = \varphi_6 H_m \quad (21)$$

$$H_{\min}' \left( \frac{dP}{dX}, P, H \right) = \min_{x,y}(h) \quad H_{\min} = \varphi_7 H_m \quad (22)$$

$$H_{\max}' \left( \frac{dP}{dX}, P, H \right) = \max_{x,y}(h) \quad H_{\max} = \varphi_8 H_m \quad (23)$$

## 2.3 Flow Factors

To couple the micro- and macro-scale models flow factors were calculated using RSM in a similar approach to that derived by de Boer, et al. [30]. The Moving Least Squares (MLS) method is used to create a multidimensional metamodel of the macro-scale variables  $\mathbf{x} = (dP/dX, P, H)$  for each of the flow factors  $\boldsymbol{\varphi}$ . Underlying the calculation of flow factors described here was that the micro-scale model can only be assessed over a range of predetermined experiments for the variables,  $\mathbf{x}$ , and the corresponding responses of the micro-scale model constructed. This is the metamodel building stage in which a Design of Experiments (DOE) is used to choose the set of micro-scale models to include over the range of variables and the data subsequently collected.

### 2.3.1 Moving Least Squares

Eqs. (1), (3), (19)-(23) show that for each output variable the flow factors are each written as the coefficients terms in a series summation, where the terms on the right-hand-side in the equations are only functions of the variables  $\mathbf{x}$  multiplied by the corresponding flow factors  $\boldsymbol{\varphi}$ . It follows that after the metamodel building stage  $\boldsymbol{\varphi}$  can be obtained by a regression type analysis of the known experiments and corresponding output data using these equations as basis functions.

MLS is a form of least squares regression where the coefficients of the series summation do not remain constant but are instead functions of the space in which the output is assessed,  $\boldsymbol{\varphi} = \boldsymbol{\varphi}(\mathbf{x})$ . In MLS a decay function is assigned to weight the influence of terms in the regression analysis, associated with the weighting is a parameter  $\theta$  known as the closeness of fit. Typically a Gaussian decay function based on the Euclidean distance between known experiments and the assessment location is used for the weights  $\psi$  as described by Eq. (24),

$$\psi_i(\mathbf{x}) = \exp(-\theta r_i^2), \quad i = 1, \dots, N \quad (24)$$

where  $r_i^2$  is the squared normalised Euclidean distance between the  $i$ 'th known experiment and assessment location  $\mathbf{x}$ , and  $N$  is the number of known experiments. The normalised Euclidean distance is obtained from Eq. (25),

$$r_i^2(\mathbf{x}) = \sum_{j=1}^{j=D} (\bar{x}_{i,j} - \bar{x}_j)^2 \quad (25)$$

where  $D = 3$  is the number of dimensions of  $\mathbf{x}$ ,  $\bar{x}_j$  is the normalised  $j$ 'th component dimension of  $\mathbf{x}$ , and  $\bar{x}_{i,j}$  is the normalised  $j$ 'th component dimension of  $\mathbf{x}$  for the  $i$ 'th known experiment. The normalisation for each of the component dimensions of  $\mathbf{x}$  is calculated by:  $[\bar{x}_{i,j}, \bar{x}_j] = ([x_{i,j}, x_j] - \min_i(x_{i,j})) / (\max_i(x_{i,j}) - \min_i(x_{i,j}))$ .

The MLS metamodel for the mass flux  $Q$  to give the flow factors  $\varphi_1$  and  $\varphi_2$  in Eq. (1) is determined by Eqs. (26) – (29),

$$\|\mathbf{A}\boldsymbol{\gamma} - \mathbf{b}\| = 0 \quad (26)$$

$$A_{i,1} = -\psi_i \frac{\rho(P_i)}{12\eta(P_i)} \left( H_i + \frac{P_i^{*'}}{k} \right)^3 \left( \frac{dP}{dX} \right)_i, A_{i,2} = -\psi_i \rho(P_i) U \left( H_i + \frac{P_i^{*'}}{k} \right) \quad (27)$$

$$\gamma_1 = \varphi_1, \gamma_2 = \varphi_2 \quad (28)$$

$$b_i = \psi_i Q_i' \quad (29)$$

where  $\mathbf{A}$  is the weighted matrix of terms,  $\mathbf{b}$  is the weighted vector of responses, and  $\boldsymbol{\gamma}$  is the vector of MLS coefficients. Eq. (26) is solved by minimising the sum of squared errors in the over-determined system of equations, this leads to the value of the MLS coefficients  $\boldsymbol{\gamma}$  whose components are the flow factors in Eq. (1), namely  $\varphi_1$  and  $\varphi_2$ . The remaining flow factors can be calculated by generating MLS based metamodels for Eqs. (5), (19) - (23) using the same formulation of Eqs. (26) – (29) for Eq. (1) as described in this subsection.

### 2.3.2 Closeness of Fit

The closeness of fit parameter  $\theta$  controls the rate of decay of the weights in the MLS metamodels,  $\theta$  therefore provides a method for calibrating the metamodel to reduce the error between the prediction and known experiments [37]. When  $\theta = 0$  all weights are unity and MLS reduces to the least squares problem, in this case the coefficients do not change as functions of the variables  $\mathbf{x}$ . As  $\theta \rightarrow \infty$  the influence of known experiments reduces to zero and the metamodel does not provide a response anywhere in the domain of  $\mathbf{x}$ .

The value of  $\theta$  must be determined for the metamodel, this is calibrated to produce the lowest error at known experiments when they are and are not included in the building phase. Various approaches for this procedure such as  $k$ -fold or leave-one-out cross-validation, see Loweth et al. [37]. For the calibrated value of  $\theta$  the MLS metamodel provides the minimum error between the approximation and known experiments. Once this is known the coefficients for each metamodel can be determined as functions of the input variables,  $\boldsymbol{\varphi} = \boldsymbol{\varphi}(dP/dX, P, H)$ , thus providing the method of flow factors for the multiscale approach.

### 2.3.3 Design of Experiments

The flow factors  $\boldsymbol{\varphi} = \boldsymbol{\varphi}(dP/dX, P, H)$  are calculated from MLS metamodels of homogenised micro-scale data which are updated as the macro-scale solution procedure progresses (see Section 3.1), each time a pressure distribution is obtained an additional check is made to the DOE. This check determines whether more experiments are needed within the known set in order to accurately describe the flow factors in the current region of interest.

At any given time in the solution procedure the distributions of the homogenised variables  $\mathbf{x} = (dP/dX, P, H)$  describe a curve within the design space of the components of  $\mathbf{x}$ , if this curve is far enough away from the set of known experiments then the additional experiments are added to the DOE and the corresponding micro-scale models assessed. In the case of the first check when no values exist in the DOE, the entire curve is added. The curve is described by Eq. (30),

$$(\partial s)^2 = \sum_{j=1}^{j=D} (\partial x_j)^2 \quad (30)$$

where  $s$  is the curve length. The curve is divided into 50 discrete points which are evenly spaced along  $s$  and the normalised distance to all known experiments determined, if this distance is greater than 1 % then the requirement for adding experiments is satisfied. The DOE used therefore evolves with the solution based on a curvilinear discretisation method.

### 2.3.4 Metamodel Calibration

After adding experiments to the DOE the MLS metamodels must be calibrated based on the newly obtained micro-scale data, if no values are added then no further calibration is required. Leave-one-out Cross Validation [37] was used in order to determine the closeness of fit  $\theta$  for each of the metamodels, in this method a range of  $\theta$  is chosen and the minimum error between the metamodel prediction and known experiments found over this range. The error is given by removing each set of values in the DOE in turn and building the metamodel based on the

reduced sets. The difference between the metamodel prediction and known value at the removed set are averaged over all sets. A range of  $0 \leq \theta \leq 2000$  was found to be sufficient to find a minimum value of the error for all metamodels investigated. Once  $\theta$  is calibrated for all metamodels the flow factors are determined as functions of the homogenised variables  $\boldsymbol{\varphi} = \boldsymbol{\varphi}(\mathbf{x})$  and used in the macro-scale solution procedure, the calibration for the metamodel of  $P^*$  is undertaken first because this parameter is used in the definition of some of the other metamodels.

### 3. METHODS AND MATERIALS

#### 3.1 Macro-Scale EHL Solution Procedure

##### 3.1.1 Smooth Surface Assumptions

In order to obtain solutions to the macro-scale problem under smooth surface assumptions,  $h_t = 0$ , an operating load per unit depth  $W/L$  was specified and the flow factors set to  $\boldsymbol{\varphi} = 1$ . The load per unit depth was obtained by solving Eqs. (2) and (4) together for the pressure and film thickness at a given value of the separation  $H_0$  and subsequently incrementing this parameter until the required value of  $W/L$  was reached (Eq. (8)). At each increment an initial value for the pressure distribution was needed which takes the solution from the previous step, for the first step a separation of  $H_0 = 0.5 \mu\text{m}$  was chosen and the initial values for the pressure distribution take the Hertz distribution  $P_0$  over the domain, see Eq. (31). The size of the increment of  $H_0$  was chosen as  $\Delta H_0 = -0.05 \mu\text{m}$ , once the load reached was greater than  $W/L$  a method of bisection was used to achieve the required separation. The EHL line contact was specified from the half-width of the Hertzian contact as  $-4a \leq X \leq 2a$  which was chosen to represent a large enough space for the contacting region. Solutions for the macro-scale pressure and film thickness from Eqs. (2) and (4) were obtained using Finite Elements, the contact region was divided into a number of elements and the equations discretised over them. The solutions to the macro-scale EHL problem were calculated using the software Comsol Multiphysics [38] in the non-dimensional form as described in Appendix A. The CPU used for this and all remaining calculations had a 4-core 3.3 GHz processor with 16 GB RAM.

$$P_0 = \begin{cases} P_h \sqrt{1 - \frac{X^2}{a^2}} & -a \leq X \leq a \\ 0 & X \leq -a \quad X \geq a \end{cases} \quad (31)$$

##### 3.1.2 Micro-Scale Effects

To obtain solutions inclusive of micro-EHL effects the same solution procedure for achieving  $W/L$  as described in Section 3.1.1 was used, the initial separation and pressure are given from smooth surface assumptions at the same  $W/L$  or a previously investigated  $W/L$  inclusive of micro-EHL effects. In Eqs. (2) and (4) the flow factors became functions of the variables solved for  $\boldsymbol{\varphi} = \boldsymbol{\varphi}(dP/dX, P, H)$ . Two additional steps were required as a result of the latter: (i) Convergence of load per unit area and film thickness; and (ii) Convergence of pressure with metamodel building. In (i) there is a circular dependency of the film thickness  $H$  in Eq. (4) with the load per unit area  $P^*$  as defined in Eq. (5). Therefore an iterative approach was taken for the value of  $P^*$  used when solving Eqs. (2) and (4) together, on each increment the solution to  $P^*$  was relaxed by a factor of 0.5 until convergence of the film thickness  $H$  was reached. In (ii) the metamodels used to determine the flow factors  $\boldsymbol{\varphi}$  are generated as the macro-scale solution progresses which means that the pressure distribution obtained from the solution of Eqs. (2) and (4) in the contact region depends upon the metamodel building phase. If additional experiments were added to the set of known experiments in the DOE then the metamodels will produce different results and therefore the solution procedure must be repeated, using the previous solution as the initial values. The macro-scale EHL problem inclusive of micro-scale effects was also calculated using Comsol Multiphysics [38] by application of Finite Elements in conjunction with Matlab [39] to give the flow factors. A flow chart of the macro-scale EHL solver including flow factors is given in Appendix B.

#### 3.2 Micro-Scale EHL Solution Procedure

Micro-scale EHL solutions were parameterised by the variables of the macro-scale model  $dP/dX, P, H$  such that for any combination of these variables and definition of topography  $h_t$  values of variables  $Q', P^{*'}, P_{\min}', P_{\max}', H^{*'}, H_{\min}',$  and  $H_{\max}'$  were given. In order to solve the micro-scale EHL model Eqs. (8) and (10) for the pressure and film thickness respectively were fully coupled with the deformation as calculated from Eqs. (14) – (16) using a quasi-static approach. Pressure calculated in the fluid domain was mapped to the solid domain, and deformation in the solid domain was mapped to the stationary coordinates of the fluid domain by linear interpolation. Each of the fluid and solid problems were solved sequentially until convergence in the pressure distribution was achieved. The initial value for pressure was set to  $p = P$  and the problem was solved by application of Finite Elements to

each of the fluid and solid problem respectively. Comsol Multiphysics [38] was used to calculate the solutions for the micro-scale EHL problem.

### 3.3 Geometry and Operating Conditions

#### 3.3.1 Macro-Scale Conditions

The parameters listed in Table 1 define the operating conditions and lubricant properties of the macro-scale models investigated. Three values of the load capacity  $W/L = 100, 125, 150$  kN/m were selected to demonstrate the response over a range of conditions, these loads represent a lightly loaded contact in which good convergence was achieved. For high loads a more stable solution procedure than that used here would be suitable, such as Habchi et al. [40] or Ahmed et al. [41], these methods would need to be combined with flow factors introduced here in order to incorporate micro-EHL effects.

Parameter	Value	Unit
$D_0$	0.59	GPa
$D_1$	1.34	1
$E$	100	GPa
$k$	1.333	GPa/ $\mu\text{m}$
$p_r$	0.198	GPa
$R$	20	mm
$U$	1	m/s
$Z$	0.4486	1
$\eta_r$	$6.31 \times 10^{-5}$	Pa.s
$\eta_0$	1	Pa.s
$\nu$	0.3	1
$\rho_0$	850	kg/m <sup>3</sup>
$W/L$	100, 125, 150	kN/m
$a$	0.215, 0.241, 0.264	mm
$p_h$	0.296, 0.331, 0.362	GPa

Table 1 – Macro-scale EHL operating conditions and lubricant properties.

The number of finite elements chosen to discretise the macro-scale domain was 1000, these were evenly-spaced and were found to produce grid independent results as shown in Section 4.2.1. The elements used in the macro-scale solution procedure were assigned 2<sup>nd</sup> order shape functions. The solver tolerances were set to  $10^{-3}$  and computed until this level of convergence was satisfied.

#### 3.3.2 Micro-Scale Conditions

The micro-scale operating conditions and lubricant properties originate from the macro-scale, however there are additional definitions required which result from the scale separation, surface topography and stiffness properties.

The micro-scale model represents a periodically repeating surface topography which is considered to be constant over the length of the macro-scale contact region, further parameterisation of the homogenised variables with those which control the definition of topography is needed to investigate cases where the periodic topography changes along the length of the contact region. An idealised surface topography is considered as described by Eq. (32),

$$h_t = \frac{\alpha}{4} \left[ \cos\left(\frac{2\pi x}{l_x}\right) + \cos\left(\frac{2\pi y}{l_y}\right) \right] \quad (32)$$

where  $\alpha$  is the topography amplitude. The values defining the size of the micro-scale subdomain and topography are listed in Table 2, which show that the scale separation requirements needed to satisfy the assumptions of the HMM are met (See Section 2.2). The micro-scale subdomain size is an order of magnitude or more smaller than the macro-scale contact region, and the stiffness per unit area  $k$  is chosen from the separation of scales. When  $\alpha = 0$   $\mu\text{m}$  the topography is zero and smooth surface assumptions apply. It is important to note that any given definition of the shape and size of topography can be used in place of the idealised topography investigated so long as the definition is periodic. For real surfaces the function  $h_t$  would be generated from the Fourier analysis of rough surface data, an idealised surface topography has been used in this study to demonstrate the performance multiscale method developed.

Parameter	Value	Dimension
$l_x$	10	$\mu\text{m}$
$l_y$	10	$\mu\text{m}$
$t$	100	$\mu\text{m}$
$\alpha$	0.1	$\mu\text{m}$

Table 2 – Micro-scale model parameters.

A 2D grid of 500 x 50 (25000 total) evenly-spaced quadrilateral elements were used for the fluid computational domain and a 3D grid of 50 x 10 x 10 (5000 total) evenly-spaced quadrilateral elements were used for the solid computational domain, these resolutions were found to produce grid independent results as demonstrated in Section 4.1.1. For both fluid and solid simulations the solver tolerances were set to  $10^{-3}$  and the elements assigned 2<sup>nd</sup> order shape functions. The micro-EHL solver reached convergence when a difference of  $10^{-3}$  was observed in the pressure distributions obtained from the last two iterations.

## 4. RESULTS AND DISCUSSIONS

### 4.1 Micro-Scale EHL Simulations

Micro-scale EHL results are presented to demonstrate: (i) a study of the mesh resolution; and (ii) an example of the micro-EHL solutions calculated as part of the macro-scale solutions.

#### 4.1.1 Mesh Resolution

In order to determine the level of discretisation required in the micro-scale simulations a grid convergence test was performed, in this test the number of elements used for the fluid and solid domains was varied parametrically according to Table 3 and the mass flux  $Q'$  produced for a specific set of conditions recorded. The result is given for the case where  $dP/dX = -32.14$  GPa/mm;  $P = 0.5317$  GPa;  $H = 1.726$   $\mu\text{m}$  in Fig. 3 and demonstrates that as the number of elements was increased the value of  $Q'$  converged to a value of 1.139 g/(m.s) at the highest resolution. This resolution was subsequently selected for all micro-scale simulations. The values of  $dP/dX$ ,  $P$ ,  $H$  chosen represent the conditions at the macro-scale for  $W/L = 125$  kN/m at the location where  $P_{\text{max}}$  is the maximum value, see Section 4.2.3.

Mesh Resolution	Number of Fluid Elements	Number of Solid Elements
1	100x10 = 1000	30x6x6 = 1080
2	200x20 = 4000	35x7x7 = 1715
3	300x30 = 9000	40x8x8 = 2560
4	400x40 = 16000	45x9x9 = 3645
5	500x50 = 25000	50x10x10 = 5000

Table 3 – Mesh resolution of the micro-scale domain.

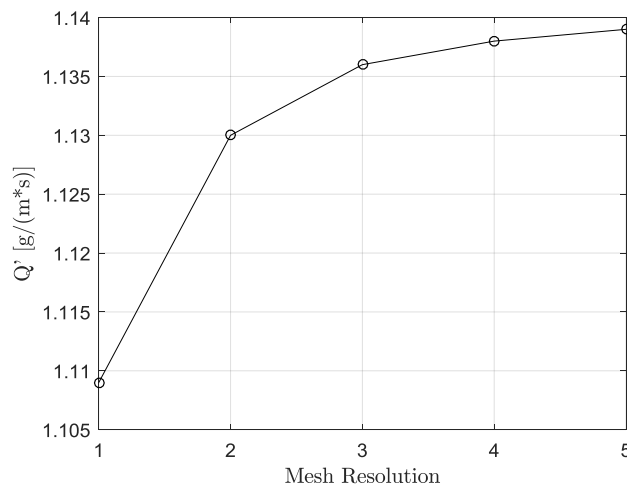


Fig. 3 – Mesh resolution study for the micro-scale simulations.

#### 4.1.2 Micro-EHL

Micro-scale distributions of pressure  $p$ , film thickness  $h$ , and the deformation  $w$  are presented in Figs. 4 – 6 respectively. These distributions correspond to the macro-scale solution for  $W/L = 125$  kN/m at which  $\overline{P}_{\max}$  is the maximum value (see Section 4.2), where  $dP/dX = -32.14$  GPa/mm;  $P = 0.5317$  GPa;  $H = 1.726$   $\mu\text{m}$ . These values were chosen to demonstrate an example micro-EHL solution used at the macro-scale.

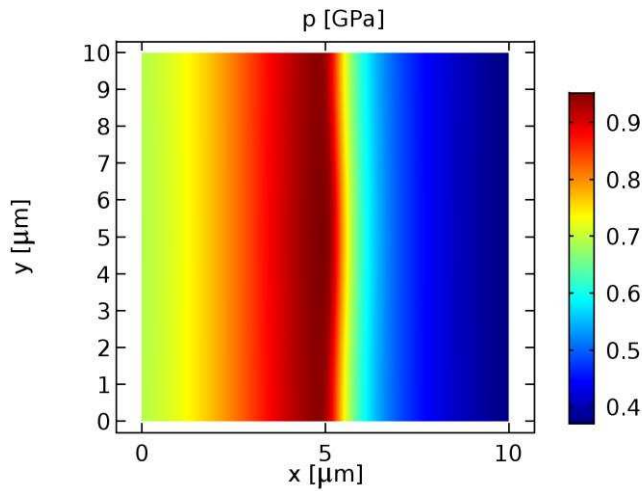


Fig. 4 – Contours of micro-scale pressure  $p$  in GPa at  $dP/dX = -32.14$  GPa/mm;  $P = 0.5317$  GPa;  $H = 1.726$   $\mu\text{m}$ .

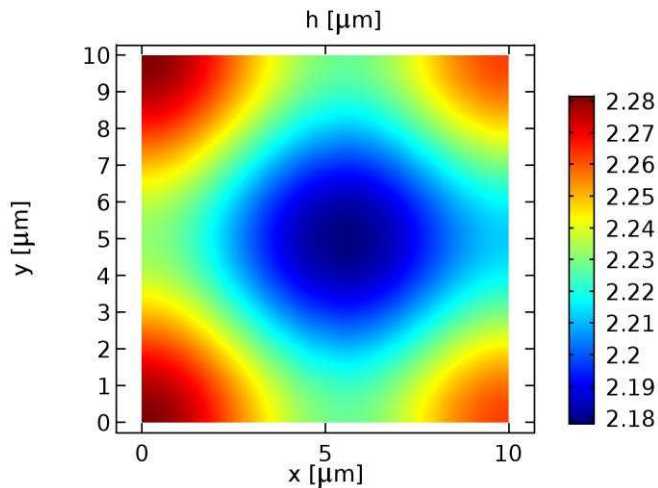


Fig. 5 – Contours of micro-scale film thickness  $h$  in  $\mu\text{m}$  at  $dP/dX = -32.14$  GPa/mm;  $P = 0.5317$  GPa;  $H = 1.726$   $\mu\text{m}$ .

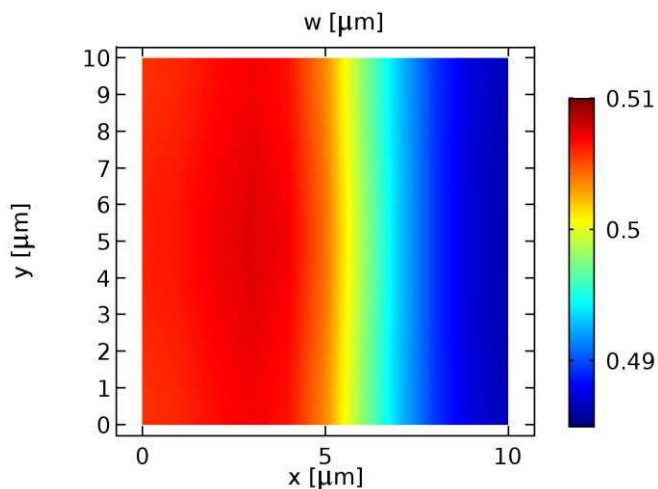


Fig. 6 – Contours of micro-scale deformation  $w$  in  $\mu\text{m}$  at  $dP/dX = -32.14$  GPa/mm;  $P = 0.5317$  GPa;  $H = 1.726$   $\mu\text{m}$ .

Fig. 4 shows an example of how pressure varies in the micro-scale subdomain. Periodicity of pressure on opposing boundaries can be observed, with a constant shift in magnitude enforced between the boundaries at  $x = 0$  and  $x = l_x$ . Within the micro-scale domain pressure fluctuates due to the presence of topography in the definition of film thickness, such that for this case  $P^* = 0.6661$  GPa which is significantly different to the constraint pressure  $P = 0.5317$  GPa. Inspecting Figs. 4 and 5 it is shown that as the fluid is driven from the inlet through the constriction where the minimum film thickness is present, there is a corresponding build up in pressure before sharply reducing at the outlet. The variation in pressure in the micro-scale domain is represented in the macro-scale in various ways using flow factors. For example  $\phi_3$  quantifies by how much load per unit area deviates from the macro-scale pressure as assumed under smooth surface assumptions.

Fluctuation in pressure in the micro-scale causes deformation to vary as presented in Fig. 6, this variation ( $\pm 0.01 \mu\text{m}$ ) represents a small proportion of the total deformation magnitude ( $0.49 \mu\text{m}$ ) which is consistent with the assumptions required by the HMM. The variation in deformation is such that the shape of topography is not significantly altered by the presence of topography under the conditions investigated, the variable  $H^* = 2.230 \mu\text{m}$  for this case which is almost identical to the value of  $H_m = 2.235 \mu\text{m}$  indicating a very small difference between the smooth surface assumptions and that inclusive of topography. In terms of flow factors this means that  $\phi_6$  is very close to 1 and the presence of topography does not significantly change the macro-scale film thickness. In the case of higher loads than those considered in this work surface topography may be flattened-up, this is not observed here but the method is also not constrained to this and as such  $H^*$  and  $H_m$  will differ. So long as the variation in deformation over the domain is smaller than the total deformation by an order of magnitude any amount of localised deformation at the micro-scale can be modelled. Plastic deformation of the surface topography may also be exhibited under higher loads, the model does not currently consider this since the separation in scales is based on the materials having linear elastic behaviour. Further development of how plastic deformation can be considered in the micro-scale model is therefore a requirement for future work.

## 4.2 Macro-Scale EHL Simulations

Macro-scale EHL simulation results are presented in three categories: (i) a mesh resolution study; (ii) comparing smooth surface assumptions with results including topography; and (iii) investigating homogenised micro-scale data at the macro-scale.

### 4.2.1 Mesh Resolution

A grid convergence study was undertaken to determine the number of elements required in the macro-scale simulations to produce accurate results. The non-dimensional mass flux  $\bar{Q}$  was calculated by parametrically varying the number of elements used in an example simulation where  $W/L = 125$  kN/m and the effects of micro-EHL were included. The dimensioned response of mass flux  $Q$  is presented in Fig. 7 and demonstrates that the value converges to  $1.139$  g/(m.s) when 1000 elements were used. This number of elements was therefore used for all macro-scale simulations as it was shown to give results independent of the level of discretisation. The size of elements required by the macro-scale is larger than that presented for the micro-scale (see Section 4.1.1). In the micro-scale topography is present and to capture the effects of the geometry many elements were required, whereas in the macro-scale the solution is homogenised and the geometry does not need the same level of discretisation. The value of the mass flux calculated at the macro-scale is the same as the micro-scale result shown in Fig. 3 for the same example simulation, this confirms that the two scales are accurately coupled using metamodelling, see Section 4.3.2.

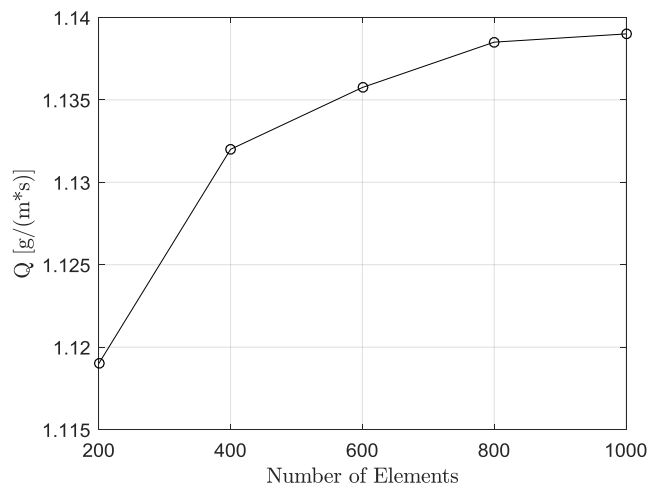


Fig. 7 – Mesh resolution study for the macro-scale simulations.

#### 4.2.2 Effect of Surface Topography

Figs. 8 – 10 illustrate the non-dimensional macro-scale pressure  $\bar{P}$  and load per unit area  $\bar{P}^*$  distributions for line contacts with and without topography, each of the figures shows this relationship for  $W/L = 100, 125, 150$  kN/m respectively.

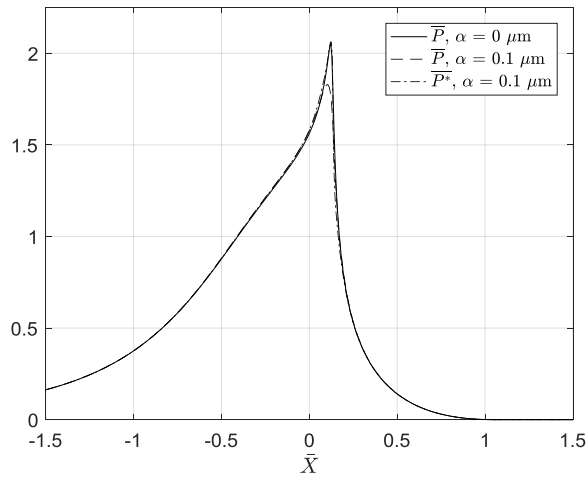


Fig. 8 – Non-dimensional macro-scale pressure and load per unit area distributions with and without topography,  $W/L = 100$  kN/m.

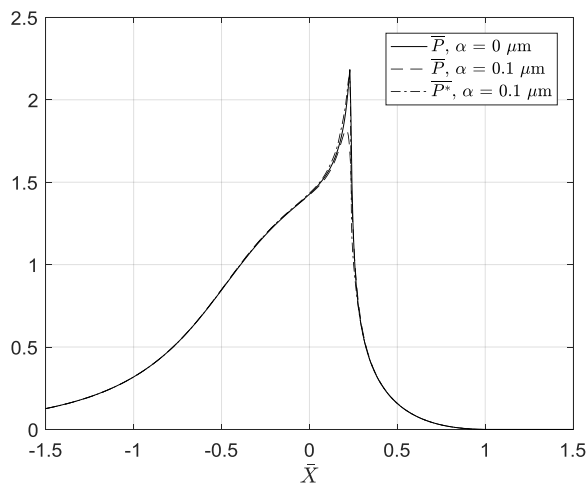


Fig. 9 – Non-dimensional macro-scale pressure and load per unit area distributions with and without topography,  $W/L = 125$  kN/m.

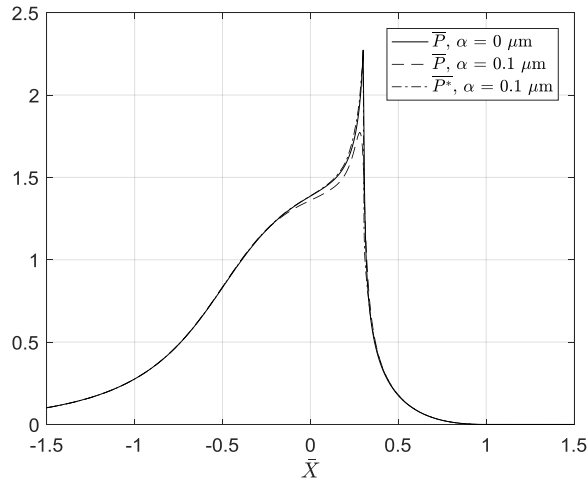


Fig. 10 – Non-dimensional macro-scale pressure and load per unit area distributions with and without topography,  $W/L= 150$  kN/m.

Under smooth surface assumptions, when  $\alpha = 0 \mu\text{m}$  and all flow factors are 1, pressure  $\bar{P}$  and load per unit area  $\bar{P}^*$  are identical whereas in Figs. 8 – 10 it is shown that when topography is included these parameters differ significantly. This effect can be attributed to the distribution of pressure in the micro-scale models used to determine the macro-scale solutions, see Section 4.1. At the micro-scale large fluctuations in pressure are observed as the lubricant flows over the surface topography, thus deviating from smooth surface assumptions. Higher pressures are generated at the macro-scale with increasing  $W/L$ , this causes larger fluctuations in the micro-scale pressure due to presence of surface topography and therefore increases the deviation from smooth surface assumptions. The load per unit area generated with topography is very similar to that generated under smooth surface assumptions, indicating that in this case the effect of topography does not significantly change the behaviour of the macro-scale solution.

Corresponding to the pressure and load per unit area distributions shown in Figs. 8 – 10 non-dimensional macro-scale film thickness  $\bar{H}_m$  distributions are presented in Figs. 11 – 13 for the same values of  $W/L$  with and without topography.

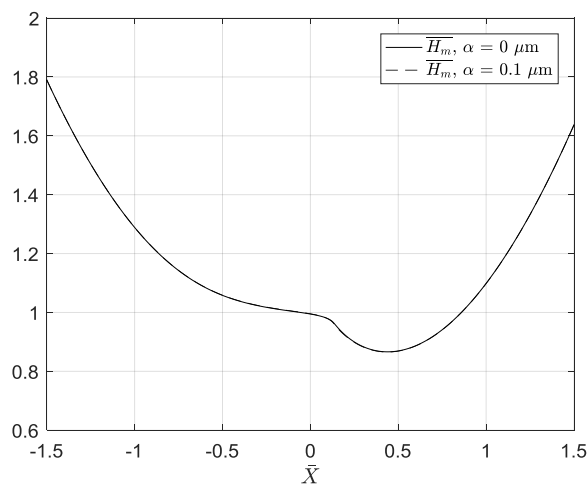


Fig. 11 – Non-dimensional macro-scale film thickness distributions with and without topography,  $W/L = 100$  kN/m.

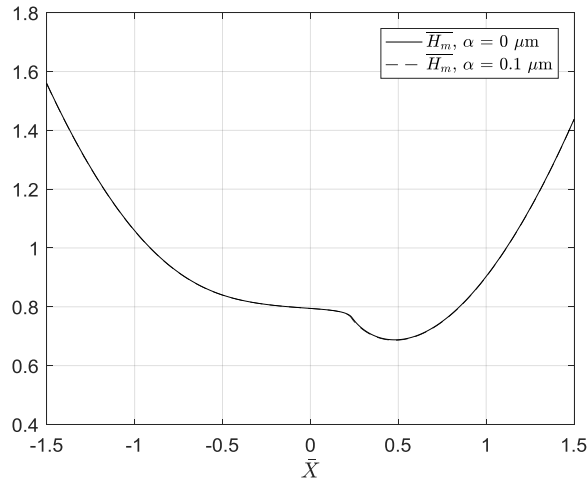


Fig. 12 – Non-dimensional macro-scale film thickness distributions with and without topography,  $W/L = 125$  kN/m.

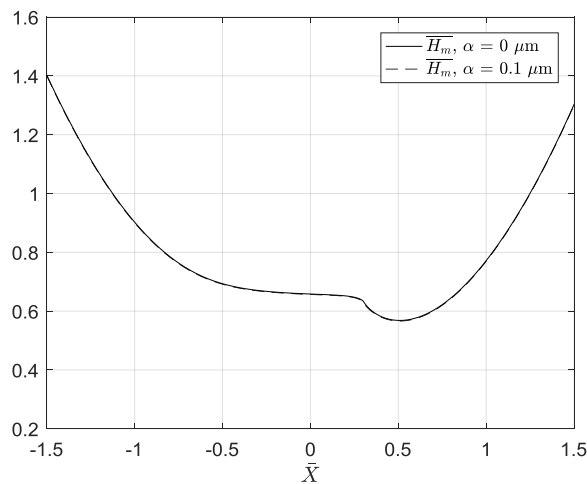


Fig. 13 – Non-dimensional macro-scale film thickness distributions with and without topography,  $W/L = 150$  kN/m.

Figs. 11 – 13 show that film thickness  $\overline{H}_m$  in the contact is not significantly different when topography is and is not modelled. This correlates to the similarity in load per unit area observed with and without topography in Figs. 8 – 10. It is also shown that an increase in  $W/L$  leads to a decrease in the macro-scale film thickness which is expected based on the known attributes of line contact problems (increasing load with decreasing separation). Overall the macro-scale solution is not significantly changed due to surface topography in comparison to smooth surface assumptions under the conditions investigated however because the multiscale solution is homogenised from the micro-scale, the method allows further investigation of micro-EHL effects which cannot be obtained from smooth surface assumptions alone (see Section 4.2.3).

#### 4.2.3 Micro-EHL

Distributions of the non-dimensional variables for pressure  $\overline{P}$ , load per unit area  $\overline{P}^*$ , minimum pressure  $\overline{P}_{\min}$ , and maximum pressure  $\overline{P}_{\max}$  are shown in Figs. 14 – 16 when topography is included, these show the micro-EHL effect in the macro-scale EHL solutions over the range of load per unit depths  $W/L = 100, 125, 150$  kN/m respectively.

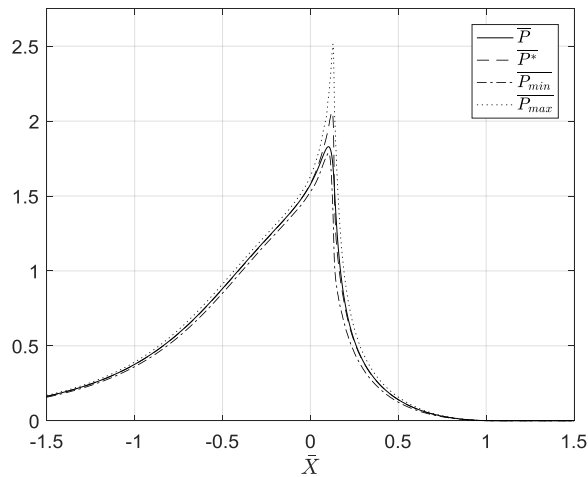


Fig. 14 – Non-dimensional macro-scale pressure, load per unit area, maximum and minimum pressure distributions at  $W/L = 100$  kN/m.

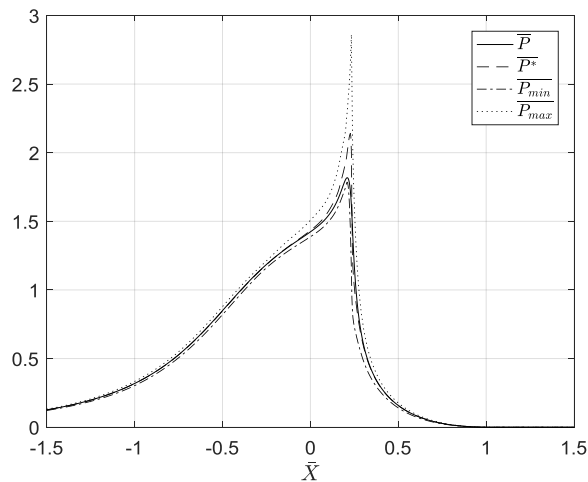


Fig. 15 – Non-dimensional macro-scale pressure, load per unit area, maximum and minimum pressure distributions at  $W/L = 125$  kN/m.

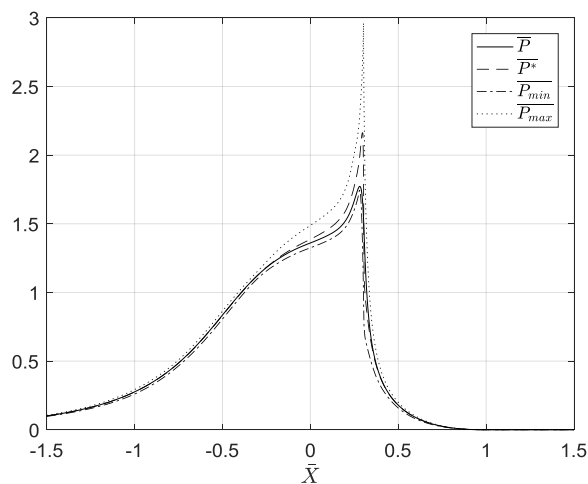


Fig. 16 – Non-dimensional macro-scale pressure, load per unit area, maximum and minimum pressure distributions at  $W/L = 150$  kN/m.

In Figs. 14 – 16 the homogenised effect of micro-scale pressure is shown for a range of macro-scale solutions, and for each of the values of  $W/L$  investigated a significant difference between the variables is observed which is

attributed the variation of pressure in the micro-scale model. As  $W/L$  is increased the differences between the maximum and minimum pressure is increased, in regions where the pressure and pressure gradient have large magnitudes a larger difference is observed. In the case where  $W/L = 150 \text{ kN/m}$   $\overline{P}_{\min}$  and  $\overline{P}$  are shown to differ by up to  $\sim 0.5 p_h$ , and  $P_{\max}$  and  $P$  differ by up to  $\sim 1.5 p_h$ . The results shown in Figs. 14 – 16 are of significant importance when considering the micro-EHL effect in the contact, the micro-scale variation of pressure represents a large proportion of the corresponding macro-scale contacting pressure.

Figs. 17 – 19 present non-dimensional macro-scale distributions for film thickness  $\overline{H}_m$ , and the homogenised variables of volume per unit area  $\overline{H}^*$ , minimum film thickness  $\overline{H}_{\min}$ , and maximum film thickness  $\overline{H}_{\max}$ . Each figure represents the same values of  $W/L$  investigated in Figs. 14 – 16.

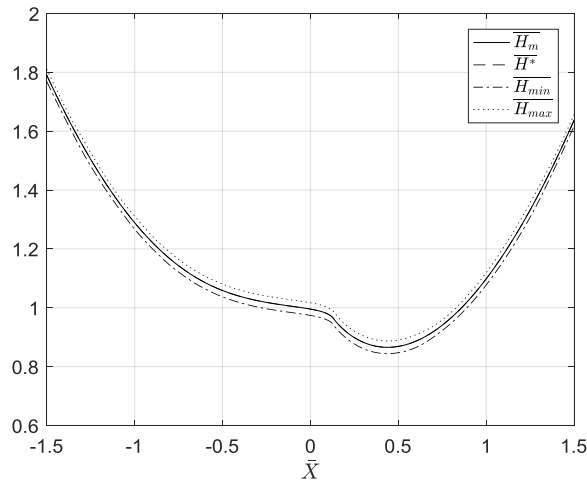


Fig. 17 – Non-dimensional macro-scale film thickness, volume per unit area, maximum and minimum film thickness distributions at  $W/L = 100 \text{ kN/m}$ .

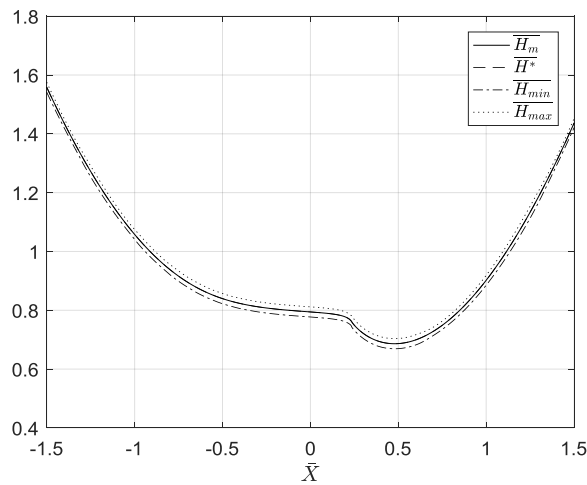


Fig. 18 – Non-dimensional macro-scale film thickness, volume per unit area, maximum and minimum film thickness distributions at  $W/L = 125 \text{ kN/m}$ .

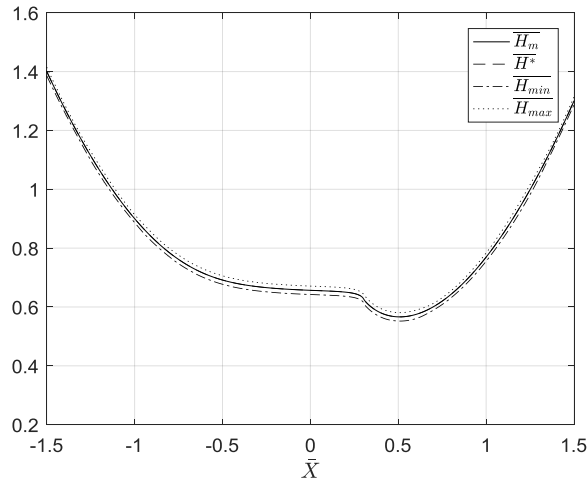


Fig. 19 – Non-dimensional macro-scale film thickness, volume per unit area, maximum and minimum film thickness distributions at  $W/L = 150$  kN/m.

Figs. 17 – 19 show that for all values of  $W/L$  that there is no significant difference between the macro-scale distributions of film thickness  $\overline{H}_m$  and volume per unit area  $\overline{H}^*$ , this implies that the average film thickness of the micro-scale model is equivalent to that at the macro-scale. It is also shown that the minimum film thickness  $\overline{H}_{min}$  and maximum film thickness  $\overline{H}_{max}$  distributions follow trends similar to that of the macro-scale film thickness but where the magnitudes are shifted by constant values. These distributions represent the bounds of the film thickness which includes the definition of surface topography modelled at the micro-scale and are of  $\pm\alpha R/2a^2$  in value respectively. These results combined indicate that the shape of topography in the micro-scale model is not significantly changed under load and that the stiffness represented by the micro-scale is equal to that represented at the macro-scale. This effect relates to the micro-scale deformation distribution shown for an example case in Fig. 6, where the variation in deformation over the micro-scale domain is significantly smaller than the total deformation magnitude. Under higher loads than observed here, significant deviation of the film thickness at the micro-scale will cause deviation of  $\overline{H}^*$  with  $\overline{H}_m$  whereby the surface topography may be flattened. Note that this is not a limitation on the method so long as the separation in scales associated with the material properties of the spring column are maintained.

### 4.3 Metamodelling

Results relating to metamodelling are divided into: (i) performance of the DOE and MLS metamodelling; (ii) comparison of macro-scale and micro-scale data; and (iii) an analysis of flow factors in the macro-scale EHL solutions.

#### 4.3.1 DOE and MLS

For each of the values of  $W/L$  investigated at the macro-scale the size and number of points added to the DOE used in calculating the flow factors are given in Table 4, also shown are the closeness of fit parameters  $\theta$  for the MLS metamodelling of  $Q$  and  $P^*$ .

W/L [kN/m]	Final DOE size	Previous DOE size	Points added to DOE	$\theta$ for Q MLS metamodel	$\theta$ for P* MLS metamodel
100	202	50	152	366	1001
125	299	202	97	555	1588
150	430	299	131	1074	1714

Table 4 – DOE and MLS metamodel parameters.

Table 4 shows that in order to provide macro-scale solutions at a given  $W/L$  a number of micro-scale experiments are required, this number is determined during the solution procedure based on the curvilinear discretisation method. Where the macro-scale solution deviates further from the initial values used more DOE points are needed, for example 152 DOE points are added to the initial 50 in order to relate the smooth surface solution to that inclusive of topography at  $W/L = 100$  kN/m, whereas only 97 relate to the  $W/L = 100$  kN/m to

the  $W/L = 125$  kN/m case because the pressure distributions are initially closer together. The evolution of the closeness of fit calibration parameter for the MLS metamodells of  $Q$  and  $P^*$  shows that as more values are added to the DOE a larger value of  $\theta$  is produced. A larger  $\theta$  will lead to more local data fitting of the MLS metamodells, implying that as more values are added to the DOE the metamodel prediction deviates further from the least squares approximation. This deviation represents a change in the behaviour of the parameters from the underlying basis functions of the MLS metamodells, which themselves describe the behaviour under smooth surface assumptions.

The curvilinear DOE approach which was generated as the macro-scale solution procedure progressed is the main difference between this method and that of de Boer et al. [29], which required 200 micro-scale simulations to be calculated before the macro-scale simulation could be started. This caused complexity in determining which experiments to choose and where to place them in the design space such that the results generated were as accurate as possible, the optimum Latin hypercube employed satisfied this argument over the entire design space. This space contained many micro-scale simulations which were far from the values used during the macro-scale solution procedure, these experiments were therefore never used due to the local data fitting nature of MLS, i.e. influence diminishing with distance from assessment location. In contrast the curvilinear DOE used in this work only adds micro-scale experiments which are close to the current macro-scale solution and as such all have an influence via the metamodel. The DOE building presented in this work is therefore a more efficient procedure than that of de Boer et al. [29] since only useful experiments are added without increasing the size beyond 200 by a large margin (up to 430 in the last case with 131 added from the initial solution), this also corresponds to an increase in the metamodel accuracy (see Section 4.3.2).

#### 4.3.2 Metamodel Performance

A comparison of the dimensioned variables calculated using flow factors at the macro-scale ( $Q$ ,  $P^*$ , etc.) with the exact corresponding micro-scale solutions ( $Q'$ ,  $P'^*$ , etc.) is presented in Table 5. Three locations along the length of the contact region are chosen for the case where  $W/L = 125$  kN/m. These locations correspond to: (i) the centre of the contact; (ii) the maximum location of  $P_{\max}$  in the contact; and (iii) the location of the minimum film thickness  $H_m$  in the contact.

$dP/dX$ [GPa/mm]	$P$ [GPa]	$H$ [ $\mu$ m]		$Q$ [g/(m*s)]	$P^*$ [GPa]	$P_{\min}$ [GPa]	$P_{\max}$ [GPa]	$H^*$ [ $\mu$ m]	$H_{\min}$ [ $\mu$ m]	$H_{\max}$ [ $\mu$ m]
1.26	0.4701	1.945	macro-scale	1.139	0.4739	0.4587	0.4984	2.301	2.255	2.352
			% error micro-scale	0.092	0.056	0.1034	-0.109	0.005	-0.030	-0.004
-32.14	0.5317	1.726	macro-scale	1.139	0.6661	0.3815	0.9461	2.230	2.184	2.281
			% error micro-scale	0.110	-0.021	0.066	-0.107	0.007	-0.052	0.087
-1.49	0.0574	1.944	macro-scale	1.139	0.0591	0.0526	0.0663	1.988	1.933	2.039
			% error micro-scale	-0.055	0.031	-0.108	0.097	-0.015	0.040	-0.022

Table 5 – Comparison of variables calculated at the macro- and micro-scales.

The errors shown in Table 5 indicate that the MLS metamodel predictions are very accurate over the length of the contact region, with the maximum discrepancy in the variables across all cases at 0.11 %. Table 5 therefore shows that the homogenised macro-scale results truly represent the micro-scale variables and that the DOE used effectively chooses the micro-scale models needed for the MLS metamodells. The level of accuracy shown in Table 3 means that the results are an order of magnitude more accurate than those generated by de Boer et al. [29] who showed errors of up to 1% between the metamodel prediction and exact corresponding micro-scale solutions.

#### 4.3.3 Flow Factors

Distributions of the flow factors  $\varphi_1$ ,  $\varphi_2$ ,  $\varphi_3$  used in determining the macro-scale parameters  $Q$  and  $P^*$  are presented in Figs. 20 – 22 for the case where topography is considered, these relate to a value of  $W/L = 125$  kN/m which is chosen to demonstrate how the flow factors vary in the contact region.

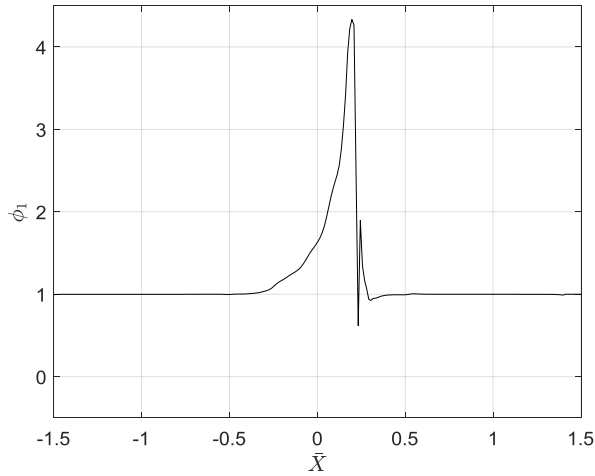


Fig. 20 – Flow factor  $\phi_1$  distribution,  $W/L= 125$  kN/m.

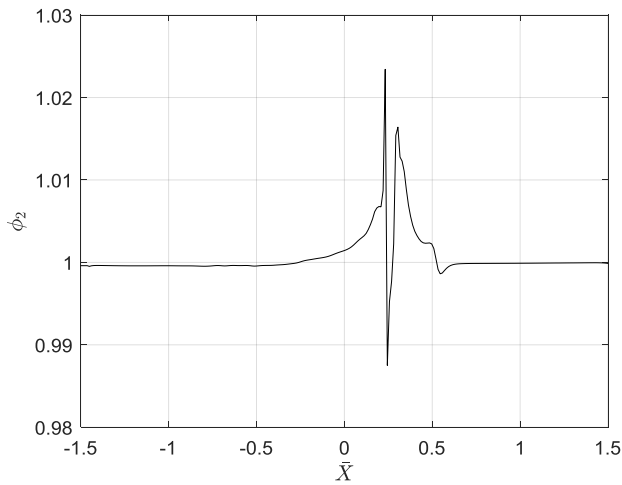


Fig. 21 – Flow factor  $\phi_2$  distribution,  $W/L= 125$  kN/m.

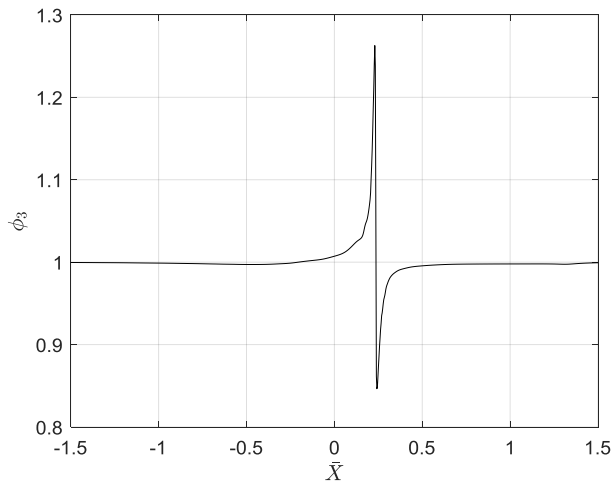


Fig. 22 – Flow factor  $\phi_3$  distribution,  $W/L= 125$  kN/m.

Figs. 20 – 22 show that in both the inlet and outlet regions of the contact that there is no significant difference between smooth surface assumptions and those inclusive of topography because the flow factors are approximately equal to 1. This is attributed to large values of  $H$  in these regions when compared to the size of topography such that the variations introduced by the micro-scale are almost negligible under these conditions. Within the region of the contact where significant differences between smooth surface solutions and those inclusive of topography are seen, the flow factors quantify the deviation of the terms of the constitutive equations.

Fig. 20 shows that the pressure gradient term of Eq. (1) deviates by up to 4.3 times that of the smooth surface solution, whereas Fig. 21 shows that the shear driven term of Eq. (1) deviates up to only 1.02 times from that of the smooth surface solution. Fig. 22 shows that load per unit area can be up to 1.25 times pressure and as low as 0.87 times pressure, which shows the significance of the difference between the two parameters. The deviations from the smooth surface solutions exhibited in Figs. 20 – 22 are nonlinear functions of the variables  $dP/dX$ ,  $P$ ,  $H$ , these distributions are non-trivial such that in order to produce them the multiscale method and subsequent metamodel approach described are required. The shape of the flow factor distributions are complex and significantly change in the region of the contact where the film thickness  $H$  is near the minimum value, at which pressure reaches the maximum value and then rapidly decreases to zero. This corresponds to large negative values of  $dP/dX$  which subsequently cause large variations of pressure  $p$  in the micro-scale, thus further deviating from the smooth surface assumptions.

#### 4.4 Model Validation

Model validation results are separated into two subsections: (i) a study illustrating the separation in scales of the multiscale method and that of a deterministic topography; and (ii) an analysis of a deterministic solution comparable with that produced using the multiscale method.

##### 4.4.1 Separation of Scales

The size of the multiscale topography investigated in this work satisfied the separation of scales required by the HMM,  $\mathcal{O}(l_x, l_y) < \mathcal{O}(2a) - 1$ . Deterministic topography which is not constrained by this difference can be modelled by assuming a macro-scale waviness in the film thickness, see for example Venner and Lubrecht [6]. Using the methodology described in this paper for the macro-scale solution procedure the EHL problem was solved with a deterministic roughness similar to that of Venner and Lubrecht [6] under steady-state conditions, a range wavelengths were investigated which decreased to the same separation in scales as demonstrated for the multiscale method in Sections 4.1-4.3. The deterministic topography is defined in the macro-scale problem by assuming all flow factors are 1 and including the additional term  $h_t$  in the film thickness equation, where  $h_t$  is given in this case by Eq. (33).

$$h_t = \frac{\alpha}{2} \cos\left(\frac{2\pi X}{l_x}\right) \quad (33)$$

The micro-scale length  $l_x$  becomes the macro-scale wavelength and this is given values of  $l_x = 100, 50, 10 \mu\text{m}$ , for which only the latter can be modelled by the multiscale method due to the required separation of scales. Figs. 23 and 24 show the macro-scale pressure and film thickness distributions obtained for the deterministic topographies, all operating conditions remained the same as specified and  $W/L = 100 \text{ kN/m}$ . Table 6 collates the number of elements, time to compute, and memory requirements for each of the cases investigated.

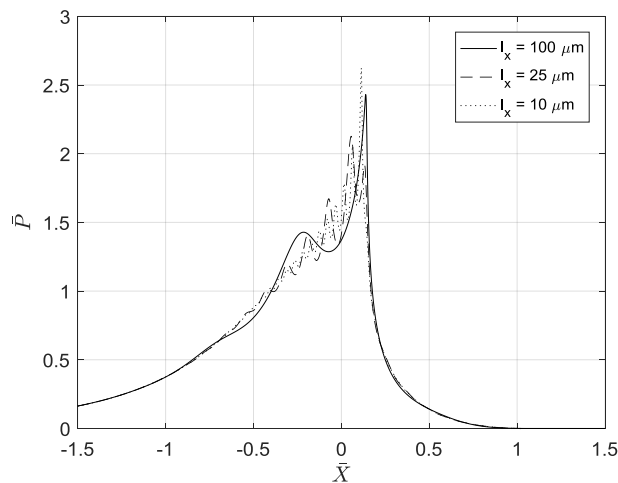


Fig. 23 – Non-dimensional macro-scale pressure distributions at  $W/L = 100 \text{ kN/m}$  calculated for a range deterministic topographies with decreasing wavelengths.

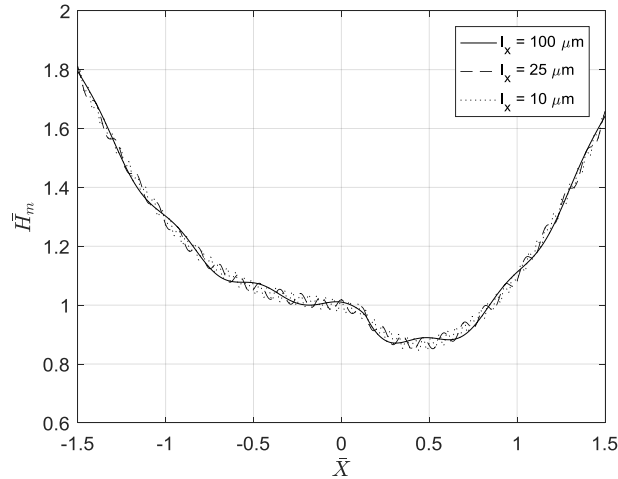


Fig. 24 – Non-dimensional macro-scale film thickness distributions at  $W/L = 100$  kN/m calculated for a range deterministic topographies with decreasing wavelengths.

Wavelength $l_x$	Number of elements	Time to compute	Memory requirements
100 $\mu\text{m}$	2500	3 hr 56 mins	3.4 GB RAM
50 $\mu\text{m}$	5000	7 hr 17 mins	6.6 GB RAM
10 $\mu\text{m}$	8000	12 hrs 3 mins	10.3 GB RAM

Table 6 – Number of elements, time to compute and memory requirements for a range of deterministic topographies decreasing wavelengths.

Fig. 23 illustrates that a waviness in the macro-scale definition of the film thickness causes ripples in the pressure distribution. This correlates well with the observations made by Greenwood and Johnson [4] who observed such effects when investigating transverse waviness in point contacts. The shape of the film thicknesses presented in Fig. 24 show that under the conditions investigated topography is not significantly changed with the waviness remaining an oscillating function along the length of the contact. As the wavelength is reduced the frequency of the pressure ripples is increased, this corresponds to the solution tending toward a mean value as the wavelength tends to zero and the smooth surface approximation is obtained. This is the same principle upon which the multiscale method is based whereby the separation in scales and periodicity of the micro-scale model allow the variables to be homogenised and coupled into the macro-scale.

Table 6 shows that as the wavelength is decreased the number of elements, time to compute and memory requirements needed to solve the problem all increase. For the case where  $l_x = 10$   $\mu\text{m}$  this is comparative to the separation in scales associated with the multiscale method. The deterministic solution at this wavelength is computationally challenging to achieve and approaching the hardware limit, this shows where the multiscale method can be useful in investigating the micro-scale effects without the associated level of discretisation.

#### 4.4.2 Deterministic and Multiscale Topography

Using Eq. (33) as the micro-scale topography definition and  $l_x, l_y = 10$   $\mu\text{m}$  the results obtained from the multiscale method were also calculated. The micro-scale out-of-plane length was arbitrarily specified as  $l_y = 10$   $\mu\text{m}$ , since there is no change in film thickness with  $y$  in Eq. (33) there will be no variation in pressure or film thickness in the micro-scale. Therefore the choice of  $l_y$  does not change the solution for the multiscale problem under this definition of topography, as such the choice of  $l_y = 10$   $\mu\text{m}$  is identical to that where  $l_y \rightarrow \infty$  which is the case for the deterministic solution. The current micro-scale model has been developed for when  $l_y$  can be given a physical value and therefore the results presented consider a more complex geometry than the deterministic counterpart in this regard. Figs. 25 and 26 respectively show the pressure and film thickness distributions obtained from the multiscale method and for the deterministic topography at  $l_x = 10$   $\mu\text{m}$ . Additionally the multiscale variables  $\overline{P_{\max}}$  and  $\overline{P_{\min}}$  have been included in Fig. 25 and  $\overline{H_{\max}}$  and  $\overline{H_{\min}}$  included in Fig. 26. The number of elements, time to compute, and memory requirements for each stage of the multiscale solution procedure are presented in Table 7.

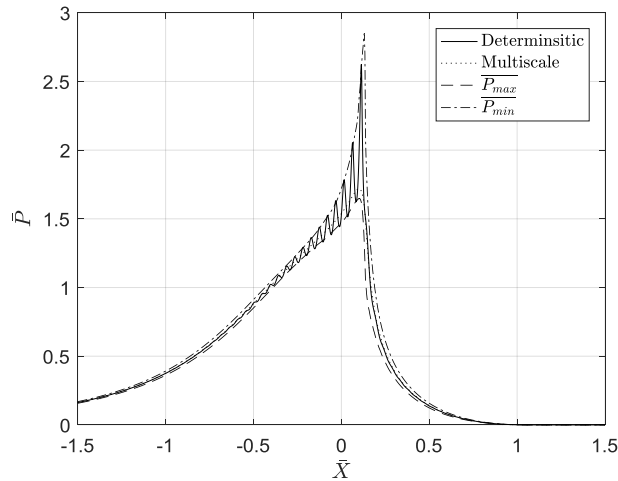


Fig. 25 – Comparison of non-dimensional macro-scale pressure distributions given by multiscale and deterministic topographies at  $W/L = 100$  kN/m.

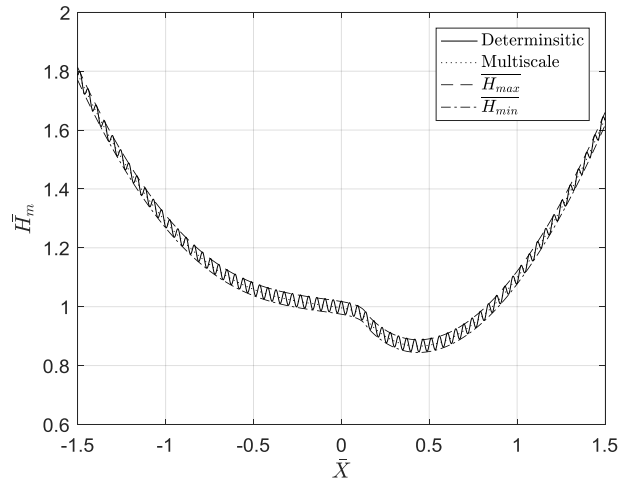


Fig. 26 – Comparison of non-dimensional macro-scale film thickness distributions given by multiscale and deterministic topographies at  $W/L = 100$  kN/m.

Stage	Number of elements	Time to compute	Memory requirements
Macro-scale	1000	1 hr 1 mins	2.1 GB RAM
Micro-scale	30000	9 hr 43 mins	3.7 GB RAM
Metamodelling	~	0 hrs 13 mins	1.9 GB RAM

Table 7 – Number of elements, time to compute and memory requirements for each stage of the multiscale solution procedure

Comparing the multiscale and deterministic topography pressure distributions in Fig. 25 shows that the multiscale solution does not exhibit ripples as observed for the deterministic solution. The solution obtained from the multiscale method does not fluctuate in the same way as the deterministic solution because pressure is homogenised at the micro-scale. Instead the variance in pressure is quantified by  $\overline{P_{max}}$  and  $\overline{P_{min}}$  which are seen to closely follow the bounds of the deterministic solution. That is when the deterministic solution fluctuates in the contact the peaks and troughs follow  $\overline{P_{max}}$  and  $\overline{P_{min}}$  respectively. This implies that the multiscale method is accurately capturing the macro-scale variation in pressure due to the micro-scale effect of surface topography. Corresponding to this Fig. 26 shows that the variables  $\overline{H_{max}}$  and  $\overline{H_{min}}$  form the bounds of the deterministic topography and the multiscale film thickness provides the mean value from which the deterministic topography oscillates. The multiscale method therefore accurately represents the macro-scale variation in film thickness due to the addition of surface topography at the micro-scale.

Table 7 shows that the total runtime was 10 hrs 57 mins for the multiscale solution, which compares to 12 hrs 3 mins for the deterministic solution and represents a decrease in the time to compute. Only 1000 elements were

required for the multiscale solution compared to 8000 in the deterministic solution, this relates to fact that the micro-scale effects are homogenised and the surface topography does not require discretisation at the macro-scale. The largest amount of time spent for the multiscale method was running micro-scale simulations, these required 30000 elements at 3.7 GB RAM and a total of 187 were run for the solution presented. The micro-scale solutions were calculated quickly with less memory when compared to the macro-scale solution but many of them were needed. The memory used in the multiscale solution was significantly less than the comparative deterministic value of 10.3 GB RAM and demonstrates another advantage of the multiscale method in modelling surface topography. It is of note that the geometry investigated in the micro-scale is more complex than the deterministic solution given the physical value assigned to the out-of-plane length scale  $l_y$ , in the case where  $l_y \rightarrow \infty$  the micro-scale solution can be reduced by a dimension and would therefore further decrease the time to compute and memory requirements of the multiscale solution.

The deterministic topography investigated in this section remains an idealised function in terms of Eq. (33) and compares well with the multiscale solution under the same conditions, thus providing a validation for the multiscale method. Real surface roughness data will change the behaviour of the responses generated by this method and require significantly more computational resource for the micro-scale simulations. By Fourier analysis of rough surface data a periodic function would be obtained from which comparisons with experimental data could be provided. It is of note that the multiscale approach is capable of modelling more complex surface topography than can be investigated deterministically at the macro-scale (full 3D effects) and is achieved without the associated additional computational cost, the multiscale method can also facilitate different constituent governing equations or material properties at the micro-scale such as the Navier-Stokes equations or shear-thinning lubricant behaviour.

## 5. CONCLUSION

This paper develops a multiscale method for solving the EHL of line contacts inclusive of surface topography based on the HMM where data is homogenised across the disparate scales of the contact. Flow factors are introduced to represent micro-EHL effects in the contacting region, which is similar in approach to the methods developed by Patir and Cheng [18] for modelling surface topography in EHL. These flow factors are calculated using MLS metamodelling based on a curvilinear discretisation method for DOE building.

Results generated using this method showed a significant increase in accuracy when compared to other papers published using the HMM for EHL. The discrepancy in the MLS metamodelling predictions were up typically 0.1% which was an order of magnitude greater than that produced by de Boer, et al. [29] who showed errors of 1% using a similar method. In order to achieve this accuracy the DOE used in this work selected experiments which were close to the values assessed during the solution procedure.

Under the conditions investigated simulations comparing smooth surface assumptions to those inclusive of topography demonstrated that there is a significant deviation when the latter is modelled, where under the conditions investigated including topography tended to reduce pressure (which differs from load per unit area due to the multiscale approach) and maintain the film thickness. The presence of surface topography in the micro-EHL model caused fluctuations of pressure and film thickness at this scale, these effects were mapped into the macro-scale solution and showed that there was a significant variation in pressure due to micro-EHL with  $\sim 2p_h$  spanning the range of values observed. Film thickness was shown not to significantly change due to micro-EHL such that the shape of topography was maintained under load. However under high loads this may not be the case and the surface topography may deviate significantly, the multiscale method is not constrained in this way and deformation of the surface feature is permitted so long as the separation in scales of the problem is maintained.

The flow factors calculated when topography was included demonstrated that there was a significant deviation in the pressure driven term of the mass flux relationship when compared to smooth surface assumptions, whereas there was a smaller change in the shear driven term. The pressure driven term was up to 4.3 times that of the smooth case whereas the shear driven term was only 1.02 times that of the smooth case. Load per unit area deviated within the range of 1.25 to 0.87 times pressure, showing the importance of defining the different terms when modelling micro-EHL effects with this method.

A study was performed comparing a deterministic topography, similar to that of Venner and Lubrecht [6], to a multiscale topography under the same conditions. The deterministic topography caused fluctuations in the pressure and film thickness similar to that observed by Greenwood and Johnson [4], whereas the multiscale topography did not due to the homogenisation of variables across the scales. The pressure ripples and surface topography modelled under deterministic conditions were shown to be accurately described by the variables spanning the bounds of the micro-scale variations in pressure and film thickness using the multiscale method.

Further development of the HMM method for EHL will include developing the micro-scale to model real roughness by decomposing experimental data into a periodic form via Fourier analysis, and by including more complex rheology and descriptions of lubricant flow such as shear-thinning and thermal transport. The macro-scale model will be developed to include a method for achieving higher load capacities such as that derived by

Habchi et al. [40] or Ahmed et al. [41], the HMM method will also be furthered to include out-of-plane lubricant flow in the macro-scale and to model the interaction of two rough deformable surfaces in contact.

## ACKNOWLEDGEMENTS

The authors wish to thank the Engineering and Physical Sciences Research Council (EP/1013733/1) and The Leverhulme Trust (F10 100/B) for funding this research.

## REFERENCES

1. Dowson D. History of tribology. Addison-Wesley Longman Limited, 1979.
2. Gohar R. Elastohydrodynamics, 2nd ed. Imperial College Press, World Scientific, 2001.
3. Etsion I. State of the art in laser surface texturing. *J Tribol* 2005;127:1:248-253.
4. Greenwood J A, Johnson K L. The behaviour of transverse waviness in sliding elastohydrodynamically lubricated contacts. *Wear* 1992;153:107-117.
5. Hooke C J. Surface roughness modification in elastohydrodynamic line contacts operating in the elastic piezoviscous regime. *J Eng Tribol*:1998;212:145-162.
6. Venner C H, Morales-Espejel G E. Amplitude reduction of small-amplitude waviness in transient elastohydrodynamically lubricated line contacts. *J Eng Tribol*:1999;213:487-504.
7. Lugt P M, Morales-Espejel G E. A review of elasto-hydrodynamic lubrication theory. *Tribol Trans* 2011;54.3:470-496.
8. Almqvist A, Dasht J. The homogenization process of the Reynolds equation describing compressible lubricant flow. *Trib Int* 2006;39:9:994-1002.
9. Larsson R. Modelling the effect of surface roughness on lubrication in all regimes. *Trib Int* 2009;42:4:512-516.
10. Mourier L, Mazuyer D, Ninove F-P, Lubrecht A. Lubrication mechanisms with laser-textured surfaces in the elastohydrodynamic regime. *Proc Inst Mech Eng-Part J: J Eng Tribol* 2010;224:697-712.
11. Zhu D, Nanbu T, Ren N, Yasuda Y, Wang Q. Model-based virtual surface texturing for concentrated conformal-contact lubrication. *Proc Inst Mech Eng- Part J: J Eng Tribol* 2010;224:685-96.
12. Gao L, Yang P, Dymond I, Fisher J, Jin Z. Effect of surface texturing on the elastohydrodynamic lubrication analysis of metal-on-metal hip implants. *Tribol Int* 2010;43:1851-60.
13. Félix-Quiñonez A, Ehret P, Summers J L. On three-dimensional flat-top defects passing through an ehl point contact: a comparison of modelling with experiments. *J Tribol* 2005;127:51-60.
14. Li J, Chen H. Evaluation on applicability of Reynolds equation for squared transverse roughness compared to CFD. *J Tribol* 2007;129:963-7.
15. Wang X, Liu Y, Zhu D. Numerical solution of mixed thermal elastohydrodynamic lubrication in point contacts with three-dimensional surface roughness. *J Tribol* 2016;139:011501.
16. Bonaventure J, Cayer-Barrioz J, Mazuyer D. Transition between mixed lubrication and elastohydrodynamic lubrication with randomly rough surfaces. *Tribol Lett* 2016;64:44.
17. Kang H, Xiong Y, Wang T, Chen Q. Research on the dynamic response of high-contact-ratio spur gears influenced by surface roughness under EHL condition. *App Surf Sci* 2017;392:8-18.
18. Patir N, Cheng H. An average flow model for determining effects of three- dimensional roughness on partial hydrodynamic lubrication. *J Tribol* 1978;100: 12-7.
19. Reynolds O. On the theory of lubrication and its application to Mr. Beauchamp Tower's experiment, including an experimental determination of the viscosity of olive oil. *Philos Trans Royal Soc Lond* 1886;177:157-234.
20. Sahlin F, Almqvist A, Larsson R, Glavatskih S. Rough surface flow factors in full film lubrication based on a homogenization technique. *Tribol Int* 2007;40:1025-34.
21. Sahlin F, Larsson R, Almqvist A, Luft P, Marklund P. A mixed lubrication model incorporating measured surface topography. Part1: theory of flow factors. *Proc Inst Mech Eng-Part J: J Eng Tribol* 2010;224:335-51.
22. de Kraker A, van Ostayen R A J, Rixen D J. Development of a texture averaged Reynolds equation. *Tribol Int* 2010;43:2100-9.
23. Tichy J, Bou-Said B. On the transition from Reynolds to Stokes roughness. In: *Transient processes in tribology*, 43. Lubrecht, Dalmaz (eds.). the Netherlands: Elsevier; 2003. p.235-42.
24. Martin S. Influence of multiscale roughness patterns in cavitated flows: Application to journal bearings. *Math Probl Eng* 2008:439319.
25. Scheichl B, Guerrieri Paleotti F S. Elasto-hydrodynamic lubrication of rough contacts: On a rigorous generalisation of the homogenisation approach. In: *Applied Sciences and Engineering (ECCOMAS 2012)*. J Eberhardsteiner, et al. (eds.). Vienna, Austria, 10-14 Sep, 2012.
26. Budt M, Temizer I, Wriggers P. A computational homogenization framework for soft elastohydrodynamic lubrication. *Comput Mech* 2012;49:749-767.
27. E W, Engquist B. The heterogeneous multi-scale methods. *Commun Math Sci* 2003;1:87-133.

28. Gao L, Hewson R W. A multiscale framework for EHL and micro-EHL. *Tribol Trans* 2012;55:713–22.
29. de Boer G N, Hewson R W, Thompson, H M, Gao L, Toropov V V. Two-scale EHL: three-dimensional topography in tilted-pad bearings. *Tribol Int* 2014;79:111-125.
30. de Boer, G N, Gao L, Hewson R W, Thompson H M, Raske N, Toropov V V. A multiscale method for optimising surface topography in elasto-hydrodynamic lubrication (EHL) using metamodels. *Struct Multidiscip Optim* 2016.
31. Gao, L, de Boer G N, Hewson R. The role of micro-cavitation on EHL: A study using a multiscale mass conserving approach. *Tribol Int* 2015;90:324-331.
32. Pérez-Ràfols F, Larsson R, Lundström S, Wall P, Almqvist A. A stochastic two-scale model for pressure-driven flow between rough surfaces. *Proc. R. Soc. A* 2016;472:20160069.
33. Cameron A. *Basic Lubrication Theory*. Longman, 1971.
34. Dowson D, Higginson G R. *Elastohydrodynamic lubrication: the fundamentals of roller and gear lubrication*. Oxford: Pergamon; 1966.
35. Roelands C. Correlational aspects of the viscosity-temperature-pressure relationship of lubricating oils [Ph.D. thesis]. Delft: Technical University Delft; 1966.
36. Benham P P, Crawford R J, Armstrong C G. *Mechanics of engineering materials*. 2nd ed. London: Pearson; 1996.
37. Loweth E L, de Boer G N, Toropov V V. Practical recommendations on the use of moving least squares metamodel building. In: Topping BHV, Tsompanakis Y, editors. *Proceedings of the 13th international conference on civil, structural and environmental engineering computing*, vol. 96, Stirlingshire: Civil-Comp Press; 2011.
38. Comsol Multiphysics [Computer Software]. 2016. Retrieved from <http://www.comsol.com>.
39. Matlab [Computer Software]. 2016. Retrieved from <http://www.mathworks.com>.
40. Habchi W, Eyheramendy D, Vergne P, Morales-Espejel G E. Stabilized fully-coupled finite elements for elasto-hydrodynamic lubrication problems. *Adv Eng Softw* 2012;46:1:4-18.
41. Ahmed S, Goodyer C E, Jimack P K. An adaptive finite element procedure for fully-coupled point contact problems. *Comp Meth App Mech Eng* 2014;282:1-21.

## NOMENCLATURE

<b>A</b>	MLS weighted matrix of terms
<b>a</b>	Half-width of Hertzian contact
<b>b</b>	MLS weighted vector of responses
<b>D</b>	Number of dimensions
$D_0, D_1$	Dowson-Higginson compressibility parameters
<b>E</b>	Young's modulus
$E'$	Reduced modulus
$H, \bar{H}$	Macro-scale film thickness, non-dimensional
$H^*, \bar{H}^*$	Volume per unit area, non-dimensional
$H_{\max}, \bar{H}_{\max}$	Maximum film thickness, non-dimensional
$H_{\min}, \bar{H}_{\min}$	Minimum film thickness, non-dimensional
$H_0, \bar{H}_0$	Separation, non-dimensional
<b>h</b>	Micro-scale film thickness
$h_t$	Surface topography
<b>k</b>	Stiffness per unit area
$l_x, l_y, l_z$	Micro-scale coordinate lengths
<b>M</b>	Longitudinal modulus
<b>N</b>	Number of known experiments
<b>n</b>	Normal surface vector
$p, \bar{p}$	Macro-scale pressure, non-dimensional
$p^*, \bar{p}^*$	Load per unit area, non-dimensional
$p_{\max}, \bar{p}_{\max}$	Maximum pressure, non-dimensional
$p_{\min}, \bar{p}_{\min}$	Minimum pressure, non-dimensional
$dP/dX, d\bar{p}/d\bar{X}$	Macro-scale pressure gradient, non-dimensional
$P_0$	Initial macro-scale pressure, non-dimensional
<b>p</b>	Micro-scale pressure
$p_h$	Hertzian contact pressure
$p_r$	Reference pressure

$Q, \bar{Q}$	Macro-scale mass flux, non-dimensional
$R$	Radius of curvature
$r$	Normalised Euclidean distance
$t$	Equivalent thickness
$s$	Curve length
$U$	Entrainment velocity
$U_1, U_2$	Velocity of lower and upper surfaces
$\mathbf{u}$	Micro-scale deformation vector
$u, v, w$	Micro-scale coordinate deformations
$W/L$	Load per unit depth
$X, \bar{X}$	Macro-scale coordinate direction, non-dimensional
$\mathbf{x}$	Vector of macro-scale variables
$\bar{\mathbf{x}}$	Vector of normalised macro-scale variables
$x, y, z$	Micro-scale coordinate directions
$Z$	Piezoviscous index
$\alpha$	Topography amplitude
$\boldsymbol{\gamma}$	Vector of MLS coefficients
$\Delta p$	Pressure difference
$\boldsymbol{\varepsilon}$	Micro-scale strain tensor
$\epsilon$	Scaling variable
$\zeta$	Scaling parameter
$\eta, \bar{\eta}$	Lubricant viscosity, non-dimensional
$\eta_r$	Reference viscosity
$\eta_0$	Ambient viscosity
$\theta$	Closeness of fit parameter
$\kappa$	Scaling parameter
$\lambda$	Lamé's first parameter
$\mu$	Shear modulus
$\nu$	Poisson's ratio
$\rho, \bar{\rho}$	Lubricant density, non-dimensional
$\rho_0$	Ambient density
$\boldsymbol{\sigma}$	Micro-scale stress tensor
$\boldsymbol{\varphi}$	Vector of flow factors
$\varphi_1, \dots, \varphi_8$	Flow factors
$\psi$	MLS weights

#### ABBREVIATIONS

DOE	Design of Experiments
EHL	Elastohydrodynamic Lubrication
FSI	Fluid-Structure Interaction
MLS	Moving Least Squares
RSM	Response Surface Methods

## APPENDIX A

Eq. (A1) gives the scaling parameters defined at the macro-scale,

$$a = \sqrt{\frac{8WR}{\pi E' L}} \quad p_h = \frac{2W}{\pi a L} \quad \frac{1}{E'} = \frac{1 - \nu^2}{E} \quad (\text{A1})$$

these are used for the non-dimensionalisation of the macro-scale variables as described by Eqs. (A2)-(A4),

$$\bar{P}, \bar{P}^*, \bar{P}_{\min}, \bar{P}_{\max} = \frac{P, P^*, P_{\min}, P_{\max}}{p_h} \quad (\text{A2})$$

$$\bar{H}, \bar{H}^*, \bar{H}_{\min}, \bar{H}_{\max}, \bar{H}_m, \bar{H}_0 = \frac{(H, H^*, H_{\min}, H_{\max}, H_m, H_0)R}{a^2} \quad (\text{A3})$$

$$\bar{X} = \frac{X}{a} \quad \bar{Q} = \frac{QR}{\rho_0 U a^2} \quad \bar{\rho} = \frac{\rho}{\rho_0} \quad \bar{\eta} = \frac{\eta}{\eta_0} \quad (\text{A4})$$

By substituting these expressions into the macro-scale governing equations Eqs. (A5)-(A7) are derived for the mass flux,

$$\bar{Q} = -\varphi_1 \epsilon \frac{d\bar{P}}{d\bar{X}} + \varphi_2 \bar{\rho} \bar{H}_m \quad (\text{A5})$$

$$\epsilon = \frac{\bar{\rho} \bar{H}_m^3}{\bar{\eta} \kappa} \quad \kappa = \frac{12 \eta_0 U R^2}{p_h a^3} \quad (\text{A6})$$

$$\frac{d}{d\bar{X}} \left[ \varphi_1 \epsilon \frac{d\bar{P}}{d\bar{X}} \right] = \frac{d}{d\bar{X}} \left[ \varphi_2 \bar{\rho} \bar{H}_m \right] \quad (\text{A7})$$

with the boundary conditions and cavitation constraints written as Eqs. (A8) and (A9),

$$\bar{P}(-\infty) = \bar{P}(\infty) = \frac{d\bar{P}}{d\bar{X}}(\infty) = 0 \quad (\text{A8})$$

$$\bar{P} < 0, \frac{d\bar{P}}{d\bar{X}} = 0 \quad (\text{A9})$$

The non-dimensional density and viscosity are given by Eqs. (A10)-(A11),

$$\bar{\rho} = \frac{D_0/p_h + D_1 \bar{P}}{D_0/p_h + \bar{P}} \quad (\text{A10})$$

$$\bar{\eta} = \exp \left[ \ln \left( \frac{\eta_0}{\eta_r} \right) \left( \left( 1 + \frac{p_h \bar{P}}{p_r} \right)^z - 1 \right) \right] \quad (\text{A11})$$

The load per unit area and film thickness are non-dimensionalised according to Eqs. (A12)-(A14),

$$\bar{P}^* = \varphi_3 \bar{P} \quad (\text{A12})$$

$$\bar{H}_m = \bar{H} + \varphi_3 \zeta \bar{P} \quad \zeta = \frac{p_h R}{k a^2} \quad (\text{A13})$$

$$\bar{H} = \bar{H}_0 + \frac{\bar{X}^2}{2} - \frac{1}{\pi} \int_{-\infty}^{\infty} (\varphi_3 \bar{P})' \ln |\bar{X} - \bar{X}'| d\bar{X}' - \varphi_3 \zeta \bar{P} \quad (\text{A14})$$

The load capacity becomes Eq. (A15),

$$\int_{-\infty}^{\infty} \varphi_3 \bar{P} \, d\bar{X} = \frac{\pi}{2} \quad (\text{A15})$$

and the remaining macro-scale parameters are given by Eqs. (A16)-(A17),

$$\overline{P_{\min}} = \varphi_4 \bar{P} \quad \overline{P_{\max}} = \varphi_5 \bar{P} \quad (\text{A16})$$

$$\overline{H^*} = \varphi_6 \overline{H_m} \quad \overline{H_{\min}} = \varphi_7 \overline{H_m} \quad \overline{H_{\max}} = \varphi_8 \overline{H_m} \quad (\text{A17})$$

Note that the flow factors  $\varphi_{1-8}$  are not changed during non-dimensionalisation from such that the relationships given exhibit the same scaling as their dimensional counterparts.

APPENDIX B

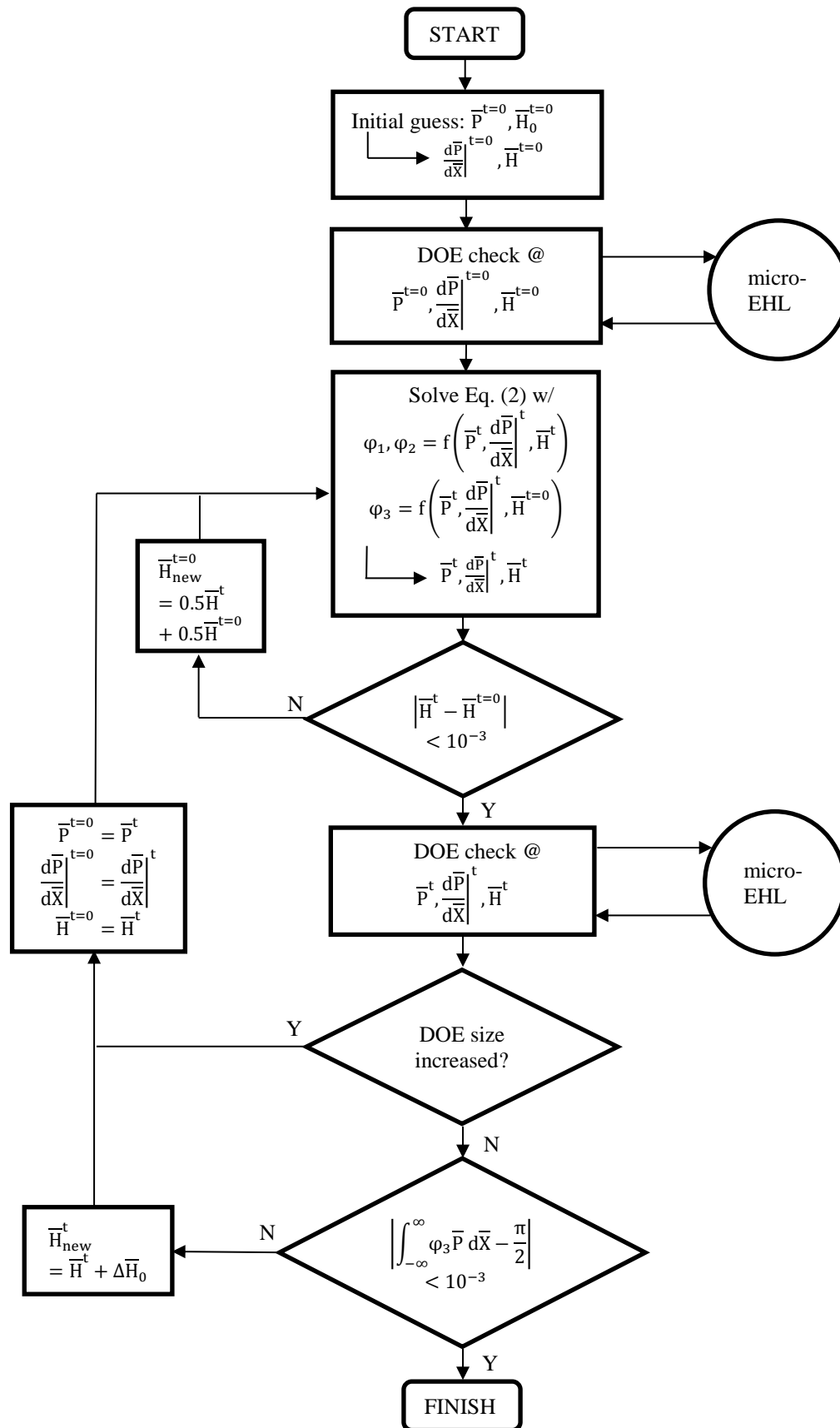


Fig. B1 – Flow chart of the macro-scale EHL solver including flow factors